The Effect of T_1 Signal Decay on Ventilation Mapping using Hyperpolarized Gas MRI during Multiple Breath Wash-out

by

Felipe Morgado

A thesis submitted in conformity with the requirements
for the degree of Master of Science

Department of Medical Biophysics
University of Toronto

The Effect of T_1 Signal Decay on Ventilation Mapping using Hyperpolarized Gas MRI during Multiple Breath Wash-out

Felipe Morgado

Master of Science

Department of Medical Biophysics
University of Toronto

2017

Abstract

Cystic fibrosis (CF) is a hereditary disease that can severely hinder lung function and cause death at a young age. Sensitive diagnostic tools are necessary to treat CF early. Hyperpolarized xenon-129 magnetic resonance imaging (HP ^{129}Xe MRI) provides a novel technique to assess regional changes in lung function by measuring signal loss through a multiple breath gas wash-out maneuver.

This thesis explores how multiple breath wash-out (MBW) imaging is confounded by T_1 signal decay. A model of T_1 as a function of wash-out breath was developed and investigated in a cohort of healthy mechanically-ventilated rats. By incorporating this model into analysis, measurements of ventilation were corrected by up to 19.3% relative to a published method that utilized a simplified approximation of T_1. Significant improvements in the accuracy of MBW imaging were observed, particularly at long time-scales and at reduced lung function. Applying this model to MBW imaging is therefore an important step towards clinical translation of the technique.

Acknowledgments

Thank you to my supervisor, Dr. Giles Santyr, for mentoring me to become a better communicator and a better scientist. My time with you has inspired me to place scientific discovery at the heart of my future career.

Thank you to my committee members, Dr. Charles Cunningham and Dr. Felix Ratjen, for the invaluable advice and criticism. Your words helped me view my research from all possible angles and with a healthy dose of skepticism.

Thank you to Dr. Marcus Couch for the guidance and patience you showed me, which encouraged me to be critical yet confident in my work.

Thank you to the other current and former members of the Santyr Lab – Brandon Zanette, Andras Lindenmaier, Yonni Friedlander, Vlora Riberdy, Elaine Stirrat, Nikhil Kanhere, and Cynthia Yeung – for all the advice and fun over the past two years.

And finally, thank you to my family and friends for the endless support. Especially, thank you to my parents for being my biggest supporters every step of the way. I could not be more fortunate.

Table of Contents

List of Tables

List of Figures

List of Abbreviations and Symbols

2D	Two-dimensional
3D	Three-dimensional
A-P	Anterior-posterior
ALARA	As Low as Reasonably Achievable
B_0	Static magnetic field
B_1	Excitation radiofrequency magnetic field
CEV	Cumulative expired volume
CF	Cystic fibrosis
CFA	Constant flip angle
CFTR	Cystic fibrosis transmembrane regulator
Cl^-	Chloride ion
CO_2	Carbon dioxide
COPD	Chronic obstructive pulmonary disease
CT	Computed tomography
E	Potential energy
^{19}F	Fluorine-19
FAVOR	Flip angle variation for offset of RF and relaxation
FEV_1	Forced expiratory volume in one second
FID	Free induction decay
FOV	Field-of-view
FRC	Functional residual capacity
FVC	Forced vital capacity
G	Gradient magnetic field
GRE	Gradient-recalled echo
$\hbar$	Reduced Planck constant
^1H	Hydrogen nucleus
^3He	Helium-3
HP	Hyperpolarized
k	Boltzmann constant
k_x, k_y, k_z	k-space coordinates
LCI	Lung clearance index
LV	Lung volume
m_S	Magnetic spin quantum number
M	Bulk magnetization
MAC	Minimum alveolar concentration
MBW	Multiple breath wash-out
MRI	Magnetic resonance imaging
n	Wash-out breath number
n^+, n^-	Number of spin-up (+) or spin-down (-) nuclei
N_2	Nitrogen
O_2	Oxygen
P	Polarization
pO_2	Partial pressure of oxygen
PET	Positron emission tomography
PFT	Pulmonary function test

r	Fractional ventilation
R	Oxygen uptake factor
Rb	Rubidium
RF	Radiofrequency
S	Signal
SD	Standard deviation
SF_6	Sulfur hexafluoride
SNR	Signal-to-noise ratio
SPECT	Single-photon emission computed tomography
SV	Specific ventilation
T_1	Longitudinal relaxation time
T_2	Transverse relaxation time
TE	Echo time
TR	Repetition time
TV	Tidal volume
UTE	Ultra-short echo time
V	Volume
VDP	Ventilation defect percent
VFA	Variable flip angle
^{129}Xe	Xenon-129
α	Flip angle
γ	Gyromagnetic ratio
Δ	Time between image acquisitions
ζ	Oxygen enhancement factor
μ	Magnetic dipole moment
τ	Inter-image delay time
ω	Angular frequency

Chapter 1

1 Motivation and Background

1.1 Overview

Cystic fibrosis (CF) is a hereditary disease with no known cure that can lead to death at a young age. Several organs are affected by CF, including the liver, the pancreas, and the lungs. Through a combination of airway obstruction, infection, and inflammation, CF hinders ventilation in a heterogeneous manner. The current standard-of-care for CF patients involves monitoring lung disease with pulmonary function tests (PFTs) such as spirometry, which have limited sensitivity to early lung disease development which are often focal in nature and not captured by a global measure mostly affected by changes in the large airways. Since early detection is crucial to CF treatment, this has motivated the development of safe functional imaging techniques that can regionally measure ventilation heterogeneity. Among these techniques, multiple breath wash-out (MBW) magnetic resonance imaging (MRI) using hyperpolarized (HP) ^{129}Xe stands out for its ability to probe poorly-ventilated regions, its high spatial resolution, and its lack of ionization radiation.

Non-wash-out sources of signal loss confound the estimation of ventilation in MBW imaging. A major confounding source is T_1 signal decay. To date, MBW imaging studies have estimated T_1 as constant, despite the fact that it changes as a function of wash-out breath number due to its dependence on the concentration of oxygen within the lungs. This is expected to limit the sensitivity of MBW imaging by over-estimating ventilation.

Motivated by the pressing need to develop a safe and sensitive regional functional imaging technique for CF patients, this thesis investigates the effect of T_1 signal decay on MBW imaging. A model for T_1 as a function of breath number is presented and investigated in a theoretical model and experimentally in a rat model. A regional measurement of lung function known as fractional ventilation (r) is acquired using this model and compared to measurements made with a simplified estimation of T_1 utilized in previously published work. This study has been submitted as a manuscript to *Magnetic Resonance in Medicine*.

1.2 Cystic Fibrosis: Prevalence, Pathophysiology and Treatment

In 2015, four of the top 10 leading causes of death worldwide were pulmonary diseases (1). Nationally, diseases and infections of the lung also have a high burden: Between 2005 and 2008, respiratory diseases and infections were the seventh and eleventh costliest diagnostic categories, respectively (2). While lung diseases are often associated with environmental causes such as smoking and air pollution, the source may also be genetic. One of the most severe hereditary diseases to affect the lungs is CF.

CF is a hereditary disorder that causes dysfunction in several organ systems and often leads to death at a young age. Predominantly found in Caucasian populations, it is caused by a collection of mutations to the CF transmembrane conductance regulator (CFTR) gene (3). The CFTR gene encodes the CFTR protein, a chloride ion (Cl^-) channel which is found within epithelial cells in organs such as the lungs and pancreas. Failure of the chloride ion channel function can prevent Cl^- from passing through the channel along its electrochemical gradient. Since the CFTR protein plays several roles in the regulation of transmembrane transport, including the regulation of other channels, vesicular transport, and osmosis, its dysregulation leads to several deleterious effects in the body (4,5). In the lungs, where CFTR expression is found in the apical membrane of epithelial cells along the airways, CF patients experience dehydration of the extracellular mucus layer due to excess reabsorption of water (4). Mucus, produced by submucosal glands and goblet cells, traps particulates such as dust from traversing deep into the lungs and obstructing the small-diameter minor airways (6). Without sufficient water, the mucus layer dries up and cannot be easily cleared from the airways by small hair-like structures known as cilia (6). The accumulation of dried mucus causes airway obstruction, inflammation - which in turn can lead to fibrosis or tissue scarring - and makes the patient much more susceptible to bacterial infection (Fig. 1.1). The precise mechanism by which CF leads to drying of the mucus layer is still debated (4,5).

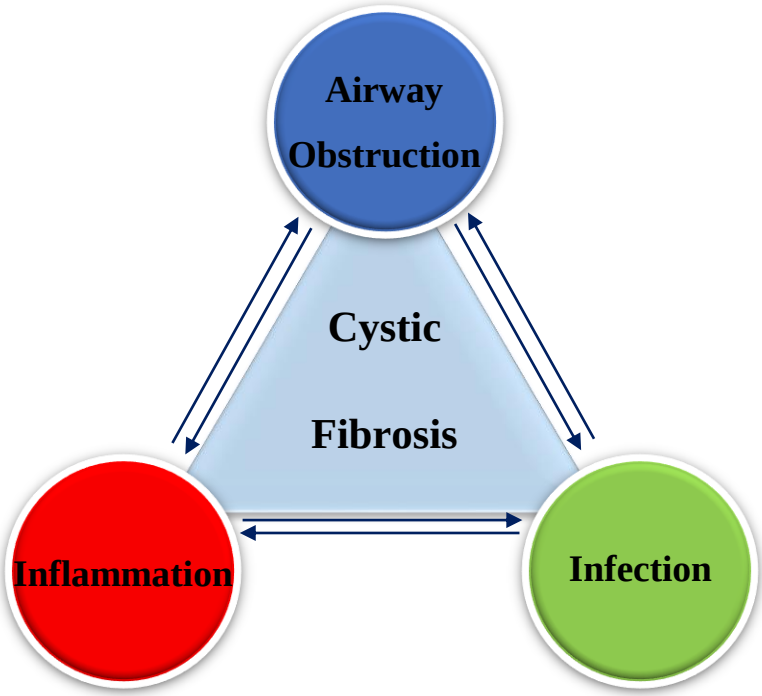

Figure 1.1: The major symptoms of CF. Each have been shown to promote the others, leading to overall deteriorating health. The hierarchy of the symptoms, including which have a greater promoter effect on the others and which tend to appear first is not widely agreed upon (4).

There is no known cure for CF, but major strides in treatment and symptom management have helped to improve survival and quality of life for CF patients. Drugs such as Ivacaftor, a potentiator that helps keep the CFTR channel open for Cl^- transport, have been developed to target CF caused by specific mutations (7). With regards to symptom management, physical therapies such as directed coughing and chest percussion – which may be performed by trained professionals or non-professional caregivers – have been demonstrated to be effective (8). Diet has also played a major role in CF care: A high-fat diet counteracts the reduced nutrient absorption experienced by patients (9). Such developments have contributed to an increase in the median age of survival (the age at which 50% of a population remains alive) of Canadian CF patients from 29.1 to 50.9 years from 1988 to 2013 (Fig. 1.2) (3).

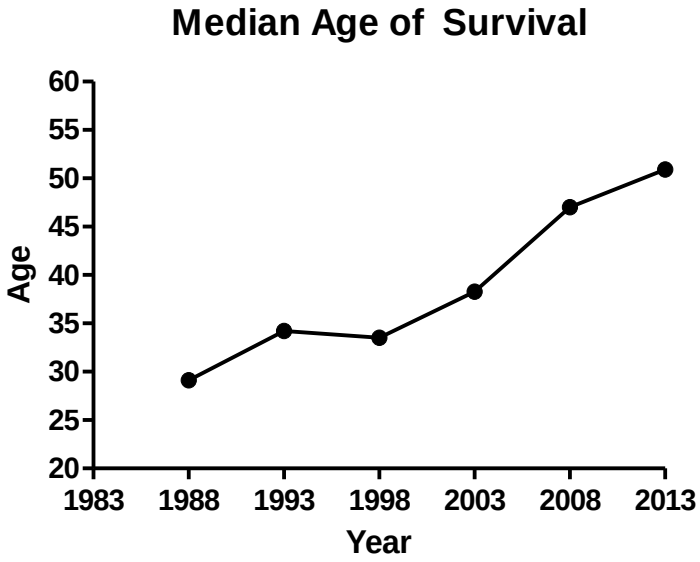

Figure 1.2: Median age of survival of Canadian CF patients. Median age of survival is defined as the estimated age at which half of a given population has died. Survival was calculated over a 5-year window. The years along the x-axis indicate the final years of windows. Adapted from (3).

Early diagnosis of CF is crucial since it allows for disease management to begin at a younger age when patients are the most vulnerable to their symptoms (10). Pulmonary function tests (PFTs) are commonly used to assess changes in lung function. Such tests are commonplace in respiratory clinics and their correlation to disease has been extensively studied (11,12). However, they are also effort-dependent, which makes them difficult to perform in patients less than 6 years of age. Furthermore, since they are global measures of lung function, their sensitivity to disease is limited (10,13). To discuss PFTs and their role in CF management in further detail, an overview of lung function and anatomy is required.

1.3 Lung Anatomy and Function

A more comprehensive treatment of pulmonary physiology can be found in John West's *Pulmonary Physiology and Pathophysiology: An Integrated, Case-Based Approach* (11). The following section is adapted from this text.

The respiratory system consists of the organs that allow gases to enter and exit the body by the process of respiration. Air enters through the oral and nasal cavities where it is humidified and filtered by small hairs in the nasal cavity which help to impede large foreign particles such as dust

from being inhaled. It then continues to move through the pharynx and larynx and into the major airways. The first major airway, the trachea, is the widest and is surrounded by rings of cartilage. The trachea divides into two bronchi, directing gas into both lungs. The bronchi then branch into the shorter and narrower bronchioles, which themselves continue to divide and decrease in size for several generations (Fig. 1.3). The first 16 generations are known as the conducting zone, while the final 7 are known as the respiratory zone. In the respiratory zone, small sacs called alveoli bud from the terminal airways. It is here that oxygen (O_2) and carbon dioxide (CO_2) are exchanged between the airspace and the pulmonary capillaries. Alveoli are conducive to gas exchange via diffusion because they are only one cell thick and have less than 1 μm of space separating them and the surrounding capillaries. Due to the highly-branched structure of the airways, the total surface area of the alveoli is estimated to be between 50 and 100 m^2. The large surface area benefits gas exchange.

The main function of the lungs is to transport O_2 and CO_2 into and out of the bloodstream via respiration. Respiration works by creating a pressure difference between the atmosphere and the thoracic cavity. Inspiration occurs due to an increase in lung volume due to contraction of the diaphragm (a muscle that sits beneath the lungs) and the intercostal muscles (muscles attached to the ribcage). According to Boyle's Law, which states that volume and pressure are inversely proportional for a constant temperature and quantity of gas, this increase in volume causes a decrease in pressure. This creates a high to low pressure gradient between the atmosphere and the lungs, drawing air inwards. Exhalation then occurs passively, meaning that muscle contraction is not required unless forced exhalation is desired.

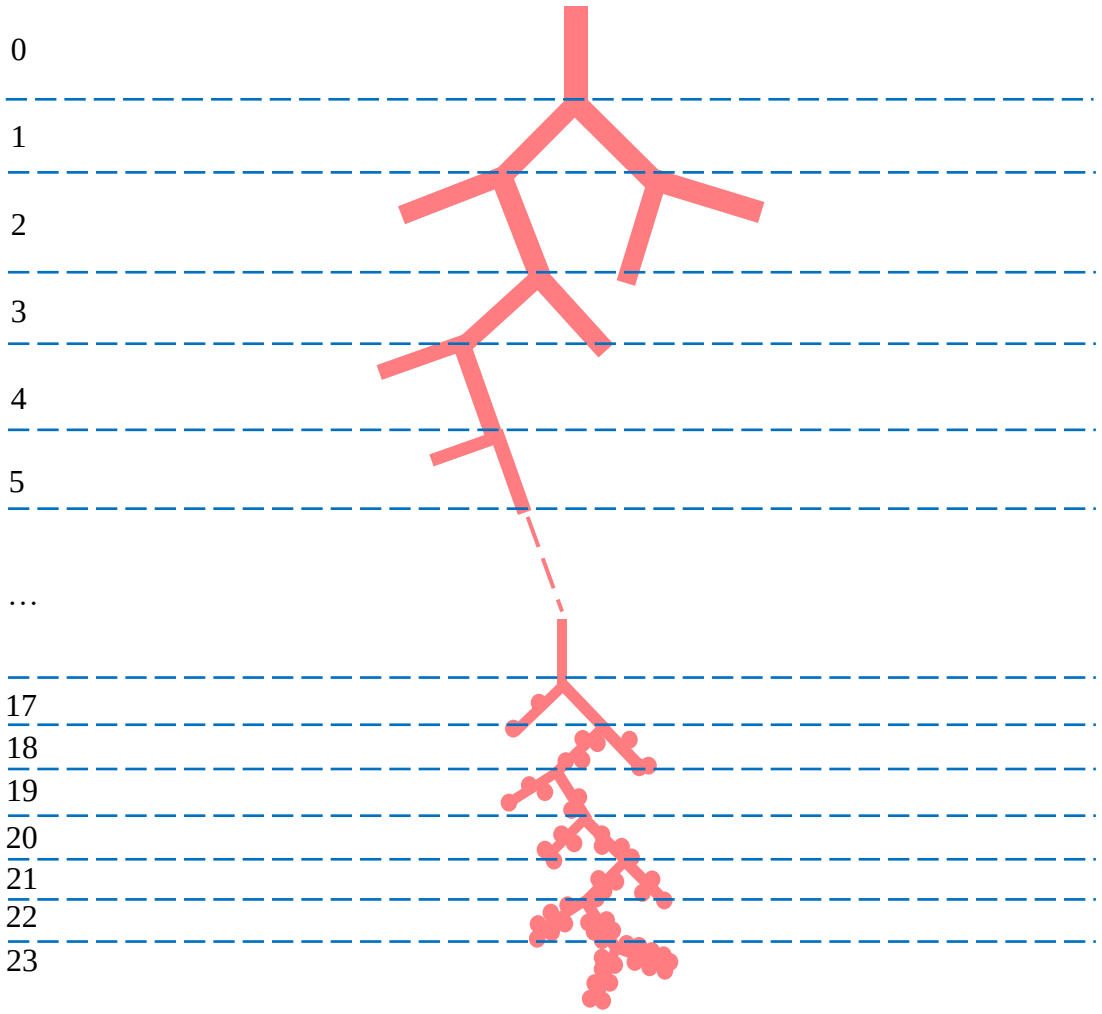

Figure 1.3: Schematic of the human airways. Airway generations are numbered along the left. Generations 0 to 16 are known as the conducting zone. The first airway in the conducting zone is known as the trachea, and it is followed by increasingly narrower airways. The conducting zone transports gas to the respiratory zone, which consists of generations 17 to 23. Gas diffuses to and from the bloodstream at the alveoli, which bud from the terminal airways in the respiratory zone. Adapted from (11).

1.4 Assessing Lung Function

1.4.1 Pulmonary Function Tests

Lung function is commonly assessed through the performance of PFTs. One widely used PFT is spirometry, in which the patient performs specific breathing maneuvers by blowing into a device known as a spirometer to measure gas volume and flow (14). Commonly defined volumes such as tidal volume, inspiratory reserve volume, and expiratory reserve volume may thus be measured. Other PFTs are required to probe the lungs' residual volume, the volume of gas which cannot be expelled by forced exhalation. Plethysmography, in which the patient is placed inside an airtight structure and lung volume is probed via a change in pressure and volume in accordance with Boyle's Law, may be used for this purpose (15). Figure 1.4 illustrates the various lung volumes that are measured with PFTs in respiratory clinics. In order to ensure consistent and comparable intra-centre and inter-centre measurements, the methodologies behind PFTs have been standardized (12).

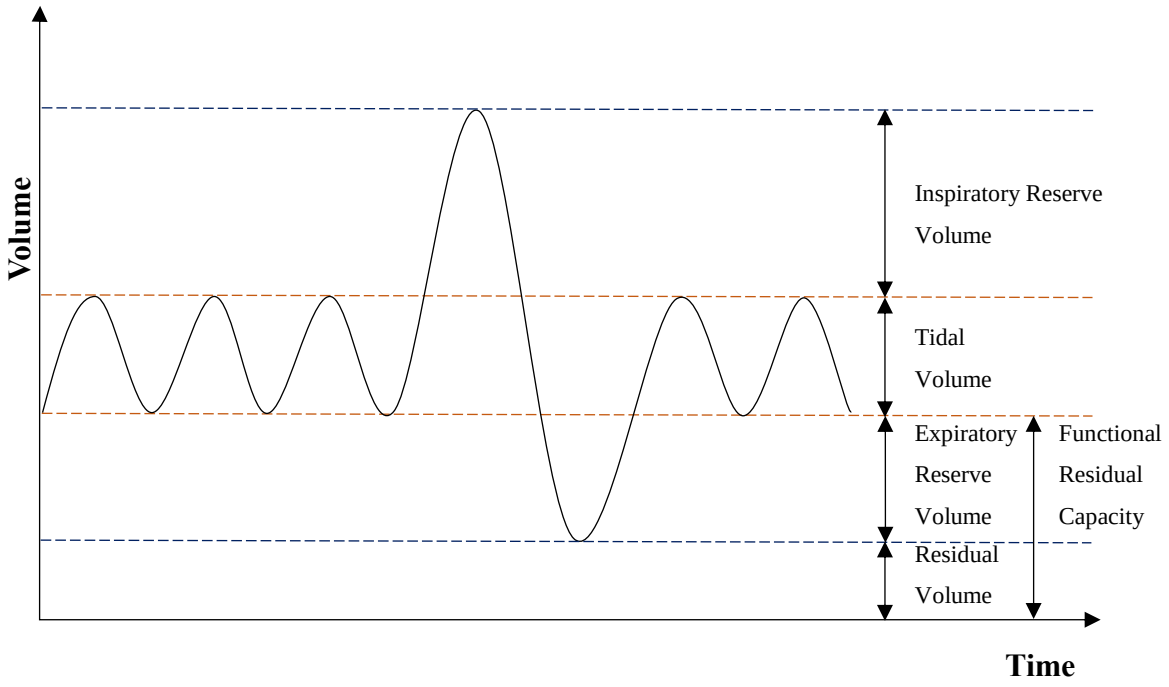

Figure 1.4: Schematic of lung volumes. Residual volume is the volume of gas within the lungs that cannot be expelled via forced exhalation. Total lung capacity is the sum of residual volume, expiratory reserve volume, tidal volume, and inspiratory reserve volume. Vital capacity is the total lung capacity minus residual volume. Volumes that include the residual volume (e.g. functional residual capacity) may be measured by plethysmography, whereas other volumes can be measured using spirometry. Adapted from (11).

One of the most commonly examined measurements of lung function for CF patients is the forced expiratory volume in one second (FEV_1) (i.e., the volume of air exhaled with maximum effort after maximum inhalation in one second (14)). FEV_1 is often reported as a percentage of $FEV_{1,pred}$, which is the predicted value based on demographic factors such as age, sex, and race (12,16). If the patient's FEV_1 is greater than or equal to 90% of $FEV_{1,pred}$, then they are considered to have normal lung function. FEV_1 can also be reported as a ratio to forced vital capacity (FVC), i.e., FEV_1/FVC. By normalizing to FVC (the total volume exhaled with maximum effort at maximum inhalation), this takes into account variations between patients' lung volumes. When airways are obstructed or narrowed, FEV_1 decreases more than FVC, leading to a reduced FEV_1/FVC. When there is airway restriction, such as when fibrosis leads to reduced compliance, FVC decreases more rapidly, leading to a normal or even elevated FEV_1/FVC (17).

FEV_1 is a quantity that is routinely measured in most PFT labs and is widely used to monitor changes in lung function with age or worsening symptoms. FEV_1 has traditionally been used to assess changes in lung function in CF patients (18); however, there are disadvantages to this. FEV_1 is an effort-dependent measurement, which hinders reproducibility and makes it difficult to assess in infants. This is noteworthy given the desire to detect and manage CF as early as possible in a patient (13). Furthermore, because of improved treatment, an increasing number of pediatric CF patients have a normal or near-normal FEV_1 (19,20). As such, FEV_1 has become a less sensitive measurement of disease manifestation. This has spurred the development of more sensitive measurements of lung function such as the lung clearance index (LCI).

1.4.2 Lung Clearance Index

LCI is a measure of lung function obtained from a PFT known as multiple breath wash-out (MBW) (21). It is attracting growing attention from physicians and pulmonary health researchers as a better metric than FEV_1 to monitor early changes in function in CF patients (20–22). The test involves measuring the concentration of a tracer gas exhaled by the patient over a series of tidal breaths through an airtight face mask. The test is finished when the concentration of the tracer gas in the expired air falls below a given fraction of its original concentration (20,22). Tracer gas concentration as a function of breath number is converted into a unitless measure of "lung volume turnovers", defined by:

$$LCI = \frac{CEV}{FRC} \quad [1.4.1]$$

; where CEV is the cumulative expired volume (corrected for dead space volume within the instrumentation) and functional residual capacity (FRC) is defined by:

$$FRC = \frac{V_{\text{net tracer}}}{c_i - c_{\text{f}}} \quad [1.4.2]$$

; where $V_{\text{net tracer}}$ is the net volume of expired tracer gas, c_{i} is the initial concentration of the tracer gas and c_{f} is its final concentration (concentrations are measured at end-exhalation of each breath). c_{f} is pre-determined to be equal to $f \cdot c_i$, where f is a fraction typically equal to 1/40 (22). FRC can also be measured by plethysmography. Originally, sulfur hexafluoride (SF_6) was the most commonly used tracer gas for LCI measurements. Patients would inhale a gas mixture containing SF_6, He, O_2 and N_2 and exhale the mixture into a mouthpiece, washing it out of their lungs with room air. The concentration of SF_6 in the expired air is measured using a mass spectrometer (13,20,23).

Over time, N_2 became increasingly popular as the tracer gas for measurement of LCI (21). MBW with N_2 is performed by having the subject breathe into a mouthpiece, exchanging air from their lungs with room air (Fig. 1.5). At a certain time-point, the gas in the MBW device is switched to 100% O_2, and N_2 in the subject's lungs is subsequently washed out during tidal breathing. N_2 concentration is indirectly measured by measuring the O_2 and CO_2 concentrations with dedicated sensors and by utilizing the known gas composition of air and Dalton's law of partial pressures (24). Because N_2 is endogenous, gas wash-out from poorly ventilated lung regions can be more thoroughly assessed. MBW with N_2 requires an airtight seal around the mouthpiece to prevent N_2 in surrounding room air from contaminating the device readings. Furthermore, the excretion of N_2 from the body into the lungs' airspace can affect measurements (20,25). LCI measurements acquired from MBW using N_2 are on average higher than LCI measurements acquired from MBW using SF_6, and that this bias becomes greater in CF patients. This is due to the difference in molecular weights and the endogenous versus exogenous nature of the two gases (20).

Figure 1.5: Preschooler performing an MBW test to measure LCI using N_2. The test was performed at The Hospital for Sick Children, Toronto, Canada.

Compared to FEV_1, there are several reasons why LCI may be a preferable measure of lung function in CF patients. Because LCI is measured through a quiet (i.e., relaxed) tidal breathing maneuver as opposed to a forced exhalation, the effort made by a patient at different tests is expected to be reproducible. LCI measurements are therefore typically more consistent than FEV_1, making it an easier measurement to acquire from young children (24,26). LCI may also be more sensitive to changes in function due to obstruction in small airways diseases such as CF (27). This is supported by longitudinal studies of the correlation between LCI and scores of computed tomography (CT) scans of the lungs, in which the CT score is a measure of disease-induced structural lung damage (22,28). Drawbacks of LCI include the risk of results being confounded by N_2 leaking into the face mask and the lack of spatial specificity. An elevated LCI may suggest increased inflammation, proliferation of airway obstructions, development of fibrosis or other changes in symptoms, but it does not indicate where symptoms are manifesting. This issue is shared with other PFTs that also lack spatial specificity. Methods that can identify regional changes in lung function may provide a greater understanding of how changes in measurements such as LCI correlate to lung disease progression. They may also be more sensitive to disease than PFTs. This type of regional information is acquired from imaging methods.

1.5 Imaging of Regional Lung Function

1.5.1 Scintigraphy, Computed Tomography & Positron Emission Tomography

Various modalities may be used to perform pulmonary imaging. This section provides a brief overview of some common tomographic techniques before focusing on the modality used in this thesis, HP gas MRI. While not discussed here, other imaging modalities that do not rely on ionizing radiation, such as optical coherence tomography, electrical impedance tomography, and ultrasound, have also been used for structural and functional lung imaging (29–31). Electrical impedance tomography and ultrasound can provide real-time bedside imaging - unlike MRI - but have lower spatial resolution than MRI (30,31). Optical coherence tomography can provide micron-level resolution of the major airways, but has low tissue penetration depth and requires sedation to insert the endoscope into the patient (29).

Pulmonary structural imaging is performed to detect anatomical changes (e.g. bronchiectasis and collapsed airways, chronic obstructive pulmonary disease (COPD)) and physical obstructions (e.g. accumulation of mucus in airways and edema) due to disease. Clinicians use these images to assess the severity of these defects and quantify them according to a scoring system (32). Most commonly, plain film x-ray is used in clinical assessments of patients. X-ray photons are transmitted towards the body and experience attenuation by interacting with tissue via phenomena such as Compton scattering and the photoelectric effect. X-rays transmitted through the other side of the body are then captured on a film, and the brightness of imaged structures is a function of attenuation. Plain film x-ray acquires 2D projection images and therefore has poor spatial resolution. To acquire 3D images of the lungs, computed tomography (CT) may be used. CT differs from plain film x-ray by directing x-ray photons towards the body in a 360^{o} sweep, which are then detected by an array of detectors. A set of 1D projections is acquired in this manner. By applying the projection-slice theorem, which states that the Fourier transform of a 1D projection through an object is equal to a slice of the 2D Fourier transform of that object along the same angle, the projections can be used to reconstruct an image of the underlying anatomy (33). The typical spatial resolution of conventional CT is on the order of 10^{-3} m. This is insufficient to capture the smallest airways, which have diameters on the order of 10^{-4} m (11). Utilizing smaller detectors and a narrower beam, recent high-resolution CT methods developed by Kakinuma et al.

attained a resolution of 1.2×10^{-4} m, though the images were noisier than those obtained by a conventional CT approach (34).

Alternative methods may image a radiodense tracer gas filling the lungs instead of the lung tissue. When a patient inhales a tracer gas, its spatial distribution within the lungs can be observed by the differences in attenuation between the exogenous tracer gas and tissue. This method is useful for locating ventilation defects by identifying regions that lack tracer gas. Xenon gas may be used in conjunction with dual-energy CT systems, which can distinguish materials based on x-ray attenuation and atomic number, to image ventilation in this manner (35).

While the foregoing methods are based on the transmission of x-ray photons, other methods are based on the emission of photons from internally introduced radionuclides. When performed with a fixed detector that acquires 2D projection images, this is known as scintigraphy. With scintigraphy, the patient inhales radioisotopes such as ^{81m}Kr and ^{127}Xe. Nuclear decay of the isotope causes the emission of gamma ray photons, which are captured by the fixed detector (36,37). If a 3D image is desired, then single-photon emission computed tomography (SPECT) would be used instead of scintigraphy. This modality relies on gamma decay of radionuclides like scintigraphy, but the gamma detectors rotate around the body being imaged, providing a set of projections for tomographic reconstruction (38). Scintigraphy and SPECT can also be used to image lung tissue perfusion. Following intravenous injection of the radionuclide, gamma ray detection as a function of blood flow can be analyzed (36,39). The absence of signal in a region can suggest the presence of a blockage in a pulmonary artery, otherwise known as a pulmonary embolism. Another radionuclide-based imaging modality known as positron emission tomography (PET) provides greater sensitivity than SPECT, but at the cost of being a significantly more expensive modality. PET differs from SPECT in that the generated gamma photons arise through positron-electron annihilation, where the positrons arising from beta decay of the radionuclide combine with local electrons and annihilate one another. The pair of gamma photons produced from the annihilation event are emitted at an angle of 180^{o} away from each other, forming a line of response that is detected by a circular array of gamma detectors. These detection events are used to image the distribution of the radionuclide in the body (40,41).

A drawback shared by the mentioned imaging modalities is that they rely on the emission of high-energy photons that can interact with DNA and introduce de novo mutations into cells,

which are then propagated through cell proliferation. These mutations accumulate and can have serious consequences such as, most notably, causing cancer. According to a 2009 report by the National Council on Radiation Protection and Measurements (42), the American population receives on average 6 mSv of radiation per person per year, half of which is due to medical procedures. Within a population, there is a 2-8% increase in fatalities caused by cancer per Sv of radiation dose experienced per year (43). Because of the health risks associated with ionizing radiation, radiologists aim to follow the ALARA principle while imaging ("As Low as Reasonably Achievable") which promotes the minimization of radiation dose administered (42). Radiation risk is elevated in young children because they undergo more rapid cell proliferation than fully grown adults and because radiation damage accumulates (44,45). Groups such as CF patients, who require constant treatment and disease monitoring throughout childhood, are especially vulnerable to radiation-induced cell damage. Furthermore, the lungs are particularly radiosensitive compared to other organs such as muscles and the liver (46). Imaging methods that do not rely on ionizing radiation are therefore sought after for pulmonary imaging of CF patients. This makes MRI an appealing modality for this aim.

1.5.2 Magnetic Resonance Imaging

1.5.2.1 Overview

A more comprehensive treatment of MRI physics can be found in Dwight Nishimura's *Principles of Magnetic Resonance Imaging* (47) and Mark Haacke, Robert Brown, Michael Thompson and Ramesh Venkatesan's *Magnetic Resonance Imaging: Physical Principles and Sequence Design* (48). The following section is adapted from these texts.

The Source of Signal: A Quantum Mechanical Description

MRI utilizes strong magnetic fields and radiofrequency (RF) fields to align, resonate, and encode precessing nuclear spins. Spin is an intrinsic property of subatomic particles that is parametrized by the spin quantum number, which defines the allowed discrete values of a particle's intrinsic angular momentum. For example, the total spin quantum number of a ^{129}Xe nucleus can only be +1/2 or -1/2. In the presence of an external magnetic field B_0 oriented along the $\hat{z}$ direction, intrinsic angular momentum along $\hat{z}$ can therefore be equal to $+\frac{1}{2}\hbar$ or $-\frac{1}{2}\hbar$, where $\hbar$ is Planck

constant divided by 2π ($\frac{h}{2\pi} = 1.054 \times 10^{-34}$ J · s). Spin also discretizes the magnetic dipole moment of particles, which is given by:

$$\boldsymbol{\mu} = \gamma \boldsymbol{S} \quad [1.5.1]$$

; where γ is the gyromagnetic ratio of a particle (i.e., the ratio of the magnetic moment to the angular momentum) and $\boldsymbol{S}$ is the spin vector. Table 1.1 provides the gyromagnetic ratio for commonly imaged nuclei in MRI. Given the abundance of water in the human body, conventional MRI measures the precession of hydrogen nuclei (^{1}H).

Nucleus	**Gyromagnetic ratio (MHz·rad·T^{-1})**	**Absolute sensitivity relative to ^{1}H**	**Natural abundance** (49)
^{1}H	267.51	1.00	99.9
^{3}He	-203.79	0.76	0.000137
^{13}C	67.26	0.25	1.07
^{19}F	251.66	0.9	100
^{129}Xe	-74.00	0.28	26.44

Table 1.1: Gyromagnetic ratio of several nuclei (47).

The sign of the spin quantum number states whether a nucleus is in a spin-up state (for spin-1/2 nuclei such as ^{1}H and ^{129}Xe, m_S = +1/2, where m_S is the magnetic spin quantum number) or in a spin-down state (m_S = -1/2). In the presence of an external magnetic field B_0, the spin states separate according to their energies. This is known as Zeeman splitting (Figure 1.6). These states can also be referred to as parallel and anti-parallel, as the spins are either aligned along or against the direction of an external magnetic field B_0. Assuming that $\boldsymbol{B} = B_0\hat{\boldsymbol{z}}$ and incorporating Eq. 1.5.1, the potential energy E of each energy sublevel is given by:

$$\begin{aligned} E &= -\boldsymbol{\mu} \cdot \boldsymbol{B} \\ &= -\gamma S_z B_0. \end{aligned} \quad [1.5.2]$$

For a spin-1/2 nucleus, $S_z = \pm\hbar/2$. The energy difference ΔE between the two sublevels generated by Zeeman splitting is given by:

$$\Delta E = \gamma \hbar B_0. \quad [1.5.3]$$

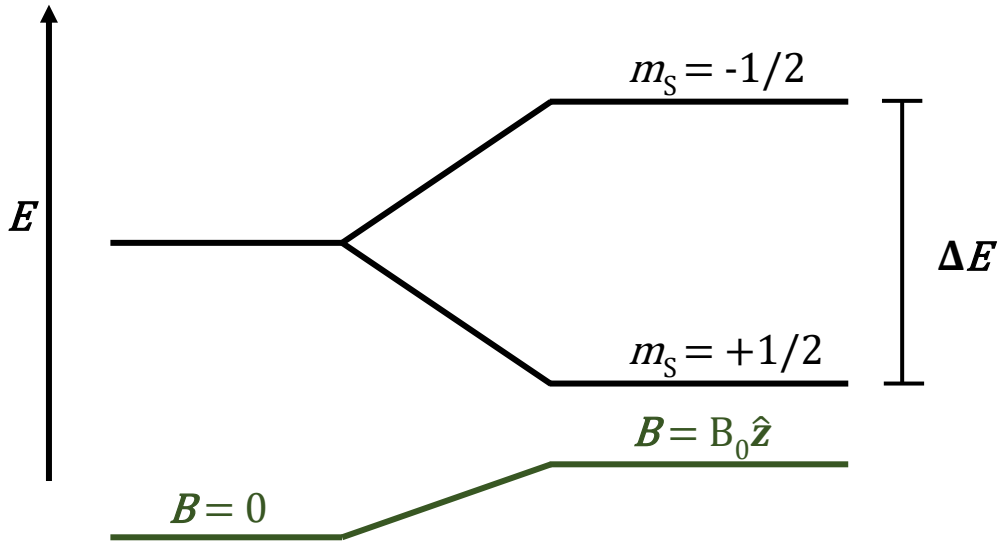

Figure 1.6: Zeeman splitting. In the absence of an external magnetic field, the spin-1/2 nuclei populate the same energy level regardless of spin state. When an external field $\boldsymbol{B} = B_0\hat{\boldsymbol{z}}$ is applied, the spins separate according to their spin states. The energy difference between the sublevels is a function of B_0 (Eq.1.5.3).

The ratio of the nuclei in spin-down state to spin-up state is a function of the energy separating the states and the temperature of the environment:

$$\frac{n^-}{n^+} = e^{-\frac{\Delta E}{kT}} \qquad [1.5.4]$$

; where k is the Boltzmann constant ($k = 1.38 \times 10^{-23}$ J/K). Polarization is defined as:

$$P = \frac{n^+ - n^-}{n^+ + n^-}. \qquad [1.5.5]$$

From Eqs. 1.5.4 and 1.5.5, it can be shown that when temperature approaches 0 K, n^-/n^+ approaches zero; therefore, $n^+ >> n^-$ and P approaches one. Conversely, at high temperatures, P approaches zero.

Signal Measurement: A Classical Mechanical Description

While knowledge of intrinsic spin is rooted in quantum mechanics, a classical mechanical perspective is helpful to understand the fundamentals of MRI. The bulk magnetization of an ensemble of nuclei is given by:

$$\boldsymbol{M} = \Sigma\boldsymbol{\mu}. \qquad [1.5.6]$$

In MRI, the aim is to detect and spatially resolve $\boldsymbol{M}$. In the absence of B_0, the nuclear magnetic moments align independently of one another in random orientations. This leads to a net $\boldsymbol{M}$ of approximately zero. If a strong, homogeneous B_0 is present in the environment of the spins, they will align with the field. The magnitude of $\boldsymbol{M}$ is dependent on n^-/n^+. If the spin populations are equal, then $\boldsymbol{M}$ equals zero. A disparity between n^- and n^+ causes $\boldsymbol{M}$ to be non-zero, creating a measurable signal. If an amplified polarization is sought (and thus greater signal), hyperpolarization methods can be applied to increase n^-/n^+ well beyond thermal equilibrium. § 1.6.3 discusses one such method known as spin exchange optical pumping.

In the presence of B_0, the magnetic dipole moment experiences a torque given by the cross product of the moment with the magnetic field, and since torque is equal to the rate of change in angular momentum:

$$\frac{d\boldsymbol{S}}{dt} = \boldsymbol{\mu} \times \boldsymbol{B} \qquad [1.5.7]$$

; where $\boldsymbol{B}$ represents the total magnetic field. Multiplying both sides by γ and summating over $\boldsymbol{\mu}$:

$$\frac{d\boldsymbol{M}}{dt} = \boldsymbol{M} \times \gamma \boldsymbol{B}. \qquad [1.5.8]$$

If $\boldsymbol{B} = B\hat{\boldsymbol{z}}$ in Eq. 1.5.8, $\boldsymbol{M}$ precesses at the frequency:

$$\omega = \gamma B. \qquad [1.5.9]$$

This is known as the Larmor frequency. To measure $\boldsymbol{M}$, it must be nutated from the $\hat{\boldsymbol{z}}$ direction into the transverse (i.e., x-y) plane by the application of a second field consisting of an oscillating RF magnetic field $\boldsymbol{B_1}(t)$. To effect the nutation, $\boldsymbol{B_1}(t)$ oscillates at the Larmor frequency that is "in resonance" with the nuclear spins. The extent to which $\boldsymbol{M}$ is transferred from the longitudinal direction into the transverse plane by the transmit RF pulse is given by the flip angle α:

$$\alpha = \int_0^t \omega_1(s) ds \qquad [1.5.10]$$

; where $\omega_1(t) = \gamma B_1(t)$.

The precessing $\boldsymbol{M}$ is measured by an RF receiver coil in the transverse plane. By Faraday's Law, the time rate of change of magnetic flux measured by the receiver coil generates an electromotive force (emf):

$$\varepsilon = -\frac{\partial \Phi_B}{\partial t}. \qquad [1.5.11]$$

The measured (or "received") emf is called the free induction decay (FID) and the collection of measured FIDs forms the signal. The decay of the magnetization occurs due to several mechanisms. The two most common mechanisms of decay are spin-lattice (i.e., longitudinal) relaxation, denoted by the time constant T_1, and spin-spin (i.e., transverse) relaxation, denoted by the time constant T_2. Incorporating these relaxation mechanisms into Eq. 1.5.8, the precession of $\boldsymbol{M}$ in a magnetic field $\boldsymbol{B}$ is given by the Bloch equation, derived by Felix Bloch in 1946:

$$\frac{d\boldsymbol{M}}{dt} = \boldsymbol{M} \times \gamma \boldsymbol{B} - \frac{M_x \hat{\boldsymbol{x}} + M_y \hat{\boldsymbol{y}}}{T_2} - \frac{M_z - M_0}{T_1} \hat{\boldsymbol{z}}. \qquad [1.5.12]$$

Signal Relaxation Mechanisms

Following the transmit $\boldsymbol{B_1}(t)$ pulse, T_1 relaxation causes $\boldsymbol{M}$ to re-establish along the longitudinal direction due to interactions between the nuclear spins and magnetic dipoles in the environment of the spins (i.e., lattice):

$$\frac{dM_z}{dt} = -\frac{M_z - M_0}{T_1}. \qquad [1.5.13]$$

The solution to Eq. 1.5.13 is:

$$M_z(t) = M_z(0) \cdot e^{-\frac{t}{T_1}} + M_0 \cdot (1 - e^{-\frac{t}{T_1}}) \qquad [1.5.14]$$

; t is the time immediately following the application of $\boldsymbol{B_1}(t)$ and M_0 is the bulk magnetization at thermal equilibrium. If a saturation pulse is used (i.e., $\alpha = 90^o$), then $M_z(0) = 0$. T_1 relaxation returns M_z to thermal equilibrium. When a hyperpolarization method is used to establish a highly nonequilibrium P in a spin ensemble prior to imaging, T_1 relaxation effectively defines the "lifetime" of the hyperpolarized state. Magnetic field fluctuations near the Larmor frequency

induce the transition of spins between the spin-up and spin-down populations and thus lead to an increased rate of T_1 relaxation (i.e., lower T_1).

Spin-spin relaxation is the dephasing of the transverse magnetization ($M_{xy} = M_x + M_y$) caused by dipole interactions between neighbouring precessing spins:

$$\frac{dM_{xy}}{dt} = -\frac{M_{xy}}{T_2}; \quad [1.5.15]$$

$$M_{xy}(t) = M_{xy}(0) \cdot e^{-\frac{t}{T_2}}. \quad [1.5.16]$$

T_2 relaxation is influenced by slow fluctuating changes in the longitudinal direction of the magnetic field, dephasing the spin ensemble and diminishing the magnitude of M_{xy}. T_2 is typically short in environments abundant in relatively static macromolecules (e.g. tissue) which have dipoles that fluctuate slower than freely moving smaller molecules (e.g. water). In practice, observed T_2 is shorter than predicted T_2 due to static magnetic field inhomogeneities that also cause signal decay. This is known as T_2* relaxation ($T_2^* \leq T_2$).

Locating Signal by Gradient Field Spin Encoding

After being tipped into the transverse plane, the bulk magnetization must be spatially and temporally encoded to perform MRI; otherwise, all that can be measured is intensity of the total signal. This is done using frequency- and phase-encoding gradients. By changing the field linearly in space, the nuclear spins can be encoded in such a way that their location can be mapped to, for instance, a Cartesian grid. When a frequency-encoding gradient is applied, the Larmor frequency of spins along a given direction becomes spatially-dependent in a linear manner:

$$\omega(x) = \omega_0 + \gamma G_x x \quad [1.5.17]$$

; where ω_0 is the Larmor frequency (rad/s), G_x is the magnetic gradient in T/m, and x is the distance along the $\hat{\boldsymbol{x}}$ direction. A phase-encoding gradient operates in a similar manner as a frequency-encoding gradient, but is turned on for a pre-determined time to induce spin dephasing along the direction of the gradient. The phases of spins when a phase-encoding gradient is applied along the y direction is given by:

$$\phi(y) = \omega(y)t_y = \left(\omega_0 + \gamma G_y y\right)t_y. \quad [1.5.18]$$

Gradients can also be used along the longitudinal direction to select a certain slice of spins to excite. If the slice thickness is given by Δz, then the corresponding bandwidth defines the range of spins excited:

$$\Delta\omega = \omega_0 + \gamma G_z \Delta z. \quad [1.5.19]$$

In a time-varying gradient field $\boldsymbol{B}(\boldsymbol{r},t) = [B_0 + \boldsymbol{G}(t)\cdot\boldsymbol{r}]\hat{\boldsymbol{z}}$ where $\boldsymbol{r} = \hat{\boldsymbol{x}} + \hat{\boldsymbol{y}} + \hat{\boldsymbol{z}}$, the solution to the Bloch equation (Eq. 1.5.12) is:

$$M(\boldsymbol{r},t) = M^o(\boldsymbol{r})\cdot e^{-\frac{t}{T_2(\boldsymbol{r})}}\cdot e^{-i\omega_o t}\cdot \exp\left(-i\gamma\int_0^t \boldsymbol{G}(\tau)\cdot\boldsymbol{r}d\tau\right) \quad [1.5.20]$$

; where $M^o(\boldsymbol{r})$ represents the initial condition and $\omega_0 = \gamma B_0$ is the Larmor frequency of the spins precessing in a magnetic field B_0.

Defining Signal

The measured signal as a function of time, $s(t)$, is the summation of all precessing spins in an imaged volume. Ignoring T_2 relaxation, and demodulating the signal by $\exp(i\omega_0 t)$, the equation for the $s(t)$ is given by:

$$s(t) = \iiint M(x,y,z)e^{-i2\pi[k_x(t)x + k_y(t)y + k_z(t)z]}dxdydz \quad [1.5.21]$$

; where $M(x,y,z)$ is the magnetization profile and $k_i(t)$ is defined as:

$$k_i(t) = \frac{\gamma}{2\pi}\int_0^t G_i(\tau)d\tau\,. \quad [1.5.22]$$

Equation 1.5.21 is identical to the 2D Fourier Transform of $M(x,y,z)$. Therefore:

$$s(t) = \mathcal{F}[m(x,y)] = \mathcal{M}\left(k_x(t), k_y(t), k_z(t)\right) \quad [1.5.23]$$

Equation 1.5.23 shows that the measured signal gives us the magnetization profile in terms of spatial frequency. The coordinates of spatial frequency are denoted by k_x, k_y, and k_z and lie in what is known as k-space. Therefore, to recover an image, an inverse Fourier transform must be applied.

Pulse Sequence Example: Gradient-Recalled Echo

Figure 1.7 shows a timing diagram for a commonly used RF pulse sequence, the gradient-recalled echo (GRE) sequence. The dotted lines under the phase-encoding gradient (G_{pe}) denote a step-wise change in gradient amplitude with each successive RF pulse excitation, and with each pulse a new line of k-space becomes encoded by the frequency-encoding gradient (G_{fe}). This samples a Cartesian grid in k-space. The negative G_{fe} and slice-select gradient (G_{ss}) lobes are applied to offset spin dephasing caused by the positive G_{fe} and G_{ss} gradients. By applying a negative gradient of identical magnitude and half the duration of the positive lobe, gradient dephasing of the spins is reversed. This creates a signal peak halfway through the application of the positive G_{fe} lobe. The time between signal generation and the peak of this refocused signal, or "echo", is called the echo time (TE).

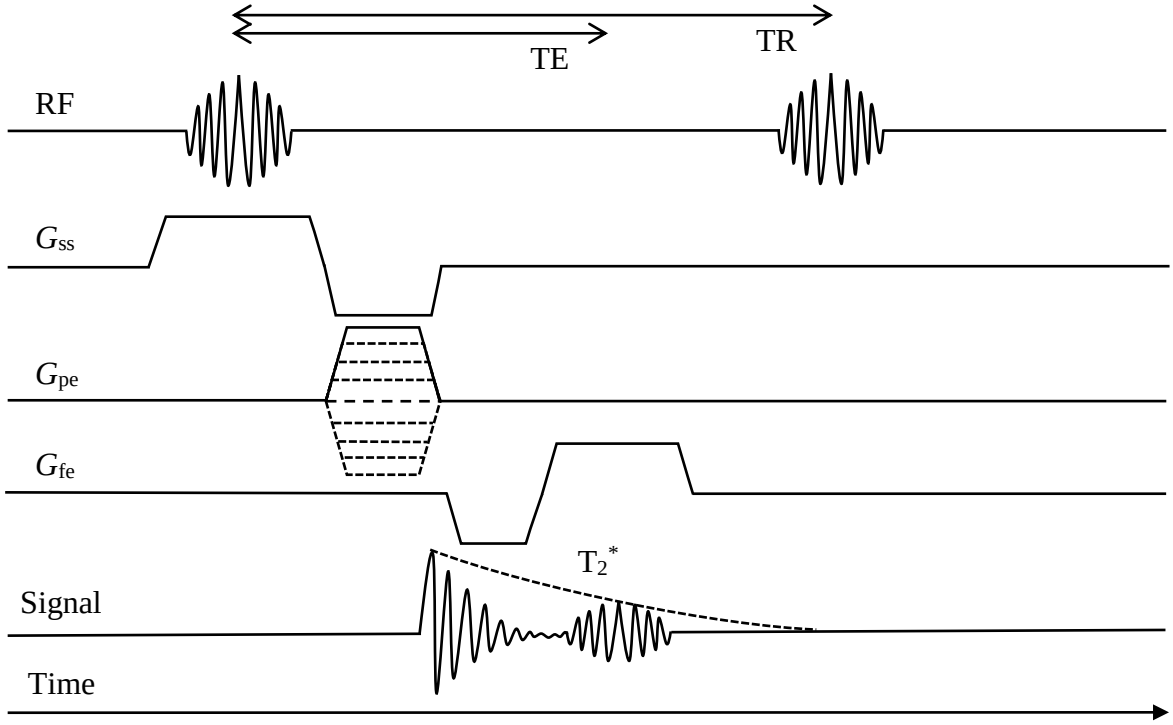

Figure 1.7: Gradient-recalled echo (GRE) pulse sequence. G_{ss} is the slice-select gradient, G_{pe} is the phase-encoding gradient, and G_{fe} is the frequency-encoding gradient. T_2^* is the relaxation rate constant due to spin-spin interactions and local magnetic field inhomogeneities. TE is the echo time and is defined as the time between the administration of an RF pulse and the peak of its signal echo. TR is the repetition time and is defined as the time between two RF pulses. The dotted lines under G_{pe} indicate a step-wise change in gradient amplitude with each successive RF pulse excitation. A GRE sequence was used in the study presented in Chapter 2. It used RF pulses with rectangular profiles in k-space and no slice selection.

1.5.2.2 ^{1}H MRI of the Lungs

As previously mentioned, conventional MRI is tuned to the resonance of ^{1}H. This is due to its abundance in the human body, which is largely composed of organic molecules and water. Unfortunately, the lungs pose a significant problem for ^{1}H MRI because unlike other organs, the ^{1}H signal is very low since the majority of lung volume is taken up by air (50). Furthermore, the airways are difficult to image due to their decreasing diameter and thickness in subsequent generations (§ 1.5.1). The thickness of structures at the alveolar level is on the order of microns; for instance, the thickness of the alveolar septum in healthy adult lung tissue is roughly 10 µm (51). This exceeds the limits of resolution demonstrated with ultra-fast ^{1}H imaging protocols which are on the order of 0.1 mm (52,53).

Another major challenge associated with ^{1}H imaging of the lungs is the extremely short T_2* of lung parenchyma (approximately 1.5 ms when imaged at 1.5 T and a voxel resolution of 1.6 mm x 3.2 mm x 10 mm) (54). This is largely due to the magnetic susceptibility difference of roughly 10 ppm between the tissue and the air within the lungs (47). Susceptibility, a measure of the magnetization of a substance when situated in an external magnetic field, is on the order of 1 – 10 ppm for most biological tissues (47). To probe the parenchyma, ultra-short echo time (UTE) MRI may be performed. UTE utilizes a sub-millisecond TE in order to probe tissues with short T_2^* (55). To shorten the TE, k-space data can be acquired using non-Cartesian phase-encoding trajectories such as spirals (Figure 1.8). Roach et al. showed that for the detection of physical abnormalities in early CF, UTE MRI strongly correlates with CT (56). To register the acquired images, a navigator echo was used to correct for organ motion due to respiration. This involved measuring the periodic change in signal intensity as a function of time at the interface of the lungs and the liver to record changes in lung volume.

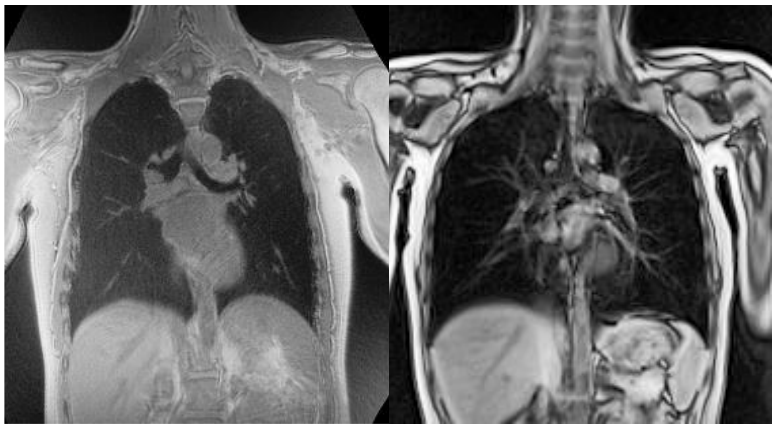

Figure 1.8: Coronal lung image of a healthy adult volunteer using a UTE sequence using a stack-of-spirals acquisition (57) (left) and a GRE sequence (right). The UTE image (TE = 50×10^{-3} ms) was acquired during free breathing, correcting for motion using a navigator echo. The GRE image (TE = 1.77 ms) was acquired during a 10 second breath-hold.

^{1}H MRI imaging methods can also be used to image pulmonary function. Oxygen-enhanced MRI takes advantage of the dependence of T_1 in the lungs on the concentration of O_2 (discussed further in § 1.7.2.1) to observe specific ventilation (SV). SV is defined as the ratio of the change in gas volume in one breath divided by the volume of gas at the end of expiration (58). Obstructions or tissue damage can cause local functional changes in the lungs, such as a diminished rate of gas wash-in or wash-out. Other functional imaging techniques using ^{1}H MRI include Fourier decomposition MRI, which temporally decomposes the measured signal according to the respiratory rate and the cardiac rate (59). These and other ^{1}H-based methods for pulmonary functional imaging face certain challenges. Notably, SNR is limited by contributions to background signal from nearby tissues. If instead a non-endogenous atomic species was imaged, the background signal problem would be eliminated. This motivates the development of hyperpolarized gas MRI.

1.6 Hyperpolarized Gas MRI

1.6.1 Overview

The lungs can be indirectly imaged by tuning MR coils to the resonant frequency of a gaseous contrast agent within the air spaces of the lung. Regional lung function information can then be obtained by observing the distribution of signal from the contrast agent. For example, a lack of signal within a region would suggest the presence of an airway obstruction. Two nuclei that are commonly used for this method are ^{3}He and ^{129}Xe (50,60).

At thermal equilibrium, a very large ensemble of spin-1/2 nuclei is necessary to generate sufficient signal since $n^- \approx n^+$ and therefore $\|\boldsymbol{M}\|$ is very small. For example, applying Eqs. 1.5.3 and 1.5.4 and assuming a temperature T = 298K and magnetic field B_0 = 3.0 T (a typical clinical field strength), n^-/n^+ for ^{1}H, ^{3}He and ^{129}Xe are 0.99979690, 1.0001547, and 1.0000561, respectively. This is acceptable for ^{1}H imaging given the abundance of the nuclei in the body. Exogenous contrast agents such as ^{3}He and ^{129}Xe gas must go through a signal-boosting process known as hyperpolarization before being introduced into the subject. Hyperpolarization is the induction of a non-equilibrium state between spin populations, amplifying the disparity between them. This process can increase the signal by a factor of 10^5 (50). Over time, the hyperpolarized (HP) gas returns to thermal equilibrium (P ~ 0) due to T_1 relaxation effects. For this reason, the signal available from HP nuclei is non-renewable, and T_1 can therefore be considered as the "lifetime" of the HP gas (further discussion is saved for § 1.6.2.1). This contrasts with ^{1}H MRI, which is performed at thermal equilibrium and therefore does not encounter this issue.

A range of anatomical and functional information can be obtained about the lungs using HP gas MRI. Loss of function in static ventilation, or the absence of gas in lung regions upon a single inhalation, can be measured as the ventilation defect percent (VDP). VDP is defined as the ratio of unventilated lung volume, as measured by the HP gas signal, to the total lung volume (61,62). Figure 1.9 compares the HP ^{129}Xe MRI scans of a healthy 14-year-old male and a 17-year-old male with CF. Ventilation defects in the CF patient are regions with an absence of ^{129}Xe signal, shown in blue. Comparing the two ventilation images, it is apparent that the CF patient has a higher VDP than the healthy subject (13% and 1%, respectively).

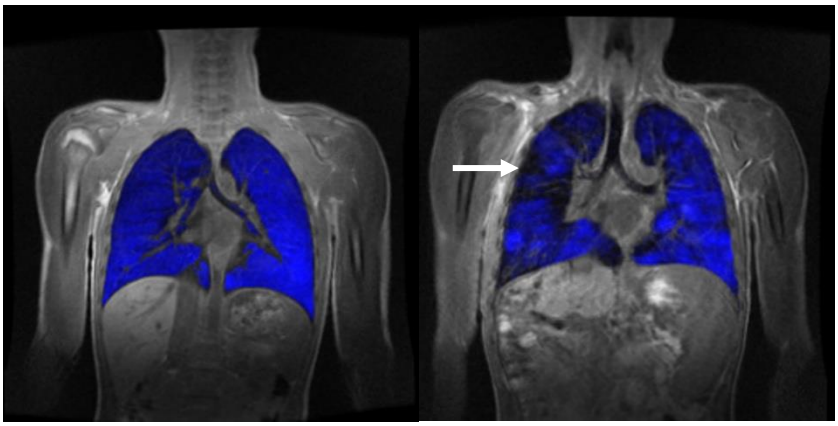

Figure 1.9: Ventilation images using HP ^{129}Xe (blue) overlaid on ^{1}H anatomical images of a healthy 14-year-old male (VDP = 1%) (left) and a 17-year-old male with CF (VDP = 13%) (right). The white arrow indicates a ventilation defect. Images were acquired at The Hospital for Sick Children, Toronto, Canada.

1.6.2 Xenon-129

To understand why ^{129}Xe is a good candidate for HP gas MRI of the lungs as well as how it interacts with the patient, a brief overview of its properties is necessary. Xenon, which comes from the Greek *xenos* meaning foreign or strange (63), is a noble gas atom and therefore has low chemical reactivity due to its full electron valence shell. It is a colourless and odourless gas that comprises 5 ppm of air (64). The ^{129}Xe isotope accounts for approximately 26% of its naturally abundant isotopes (65). In medicine, xenon gas can be used as an anesthetic agent, binding to N-methyl-D-aspartate receptors found on neurons to induce anesthetic effects (66). The amount of anesthetic agent required to induce anesthesia in 50% of patients is known as the minimum alveolar concentration (MAC). MAC is expressed as a percentage by pressure of end-expiratory gas at 1 atmosphere. The MAC of xenon is 71%, which is significantly higher than the concentration used for MRI (~10% of total lung capacity). Compared to other gaseous general anesthetics, this is smaller than nitrous oxide but considerably larger than isoflurane and its derivatives (64,67,68).

Xenon is lipophilic and capable of dissolving in tissue (69). It is also soluble in blood, and the ratio of the concentration of xenon in blood to its concentration in gas in dynamic equilibrium, otherwise known as the Ostwald solubility coefficient, is approximately 0.12 (70).

When ^{129}Xe diffuses into an environment such as the lung parenchyma, it experiences a shift in its resonance frequency known as a chemical shift:

$$\sigma\,[\text{ppm}] = \frac{\omega_{shift} - \omega_{ref}}{\omega_{ref}} \times 10^6 \qquad [1.6.1]$$

; where ω_{shift} is the Larmor frequency of ^{129}Xe shifted by local changes in the magnetic field due to the chemical environment and ω_{ref} is the reference frequency. If ^{129}Xe gas signal from the airspace is used as the reference peak in spectroscopy, then the resonant frequency of ^{129}Xe in tissue and plasma is shifted by 197 ppm and the resonant frequency of ^{129}Xe bound to erythrocytes in the blood is shifted by 217 ppm (71). Because of this chemical shift, it is possible to probe and distinguish blood, tissue, and airspace compartments. An application of this capability is assessing tissue/gas barrier thickening at the alveoli due to inflammation caused by radiation-induced lung injury (72).

^{129}Xe and ^{3}He are the two most commonly studied gases for HP gas MRI, but recently ^{129}Xe has become the favoured gas for this application. Table 1.2 compares key characteristics of both gases. ^{3}He provides greater signal than ^{129}Xe for the same number density due to a larger gyromagnetic ratio. It has been suggested that ^{3}He also more completely probes lung volume than ^{129}Xe due to its smaller size and gas viscosity (73); conversely, due to its larger size, ^{129}Xe may be more sensitive to defects. A major disadvantage of ^{3}He is that it is much more scarce and therefore more expensive than ^{129}Xe, making it less likely to be widely adopted as a clinical tool (74). ^{3}He is also unable to probe non-airspace regions as it has an Ostwald solubility coefficient 20 times smaller than ^{129}Xe (75). This thesis focuses on ^{129}Xe.

	^{3}He (76)	**^{129}Xe** (77)
Molecular weight (g/mol)	3.016	128.905
D (m^2/s) – dilute gas in air	0.86	0.14
$\frac{\gamma}{2\pi}$ (MHz/T)	-32.4	-11.8
Natural abundance (%)	0.0001	26

Table 1.2: Characteristics of ^{3}He and ^{129}Xe. In the lungs, diffusivity is normally parametrized as the apparent diffusion coefficient since diffusion is restricted by the geometry of the airways and alveoli.

1.6.3 Spin Exchange Optical Pumping

Due to the low density of gases compared to tissues, the polarization of ^{129}Xe must be amplified to have sufficient signal for imaging. The technique used to hyperpolarize ^{129}Xe in this thesis is known as spin exchange optical pumping (SEOP). In a glass cell, an alkali-metal vapor such as rubidium (Rb) is subjected to a static magnetic field created by a pair of Helmholtz coils. This magnetic field causes the ground state (5s) valence electrons of Rb to separate into two sub-levels based on their intrinsic spin (m_s = -1/2 and m_s = +1/2). This is known as the Zeeman effect (78). Using a laser emitting circularly polarized light, the m_s = -1/2 nuclei are excited to the m_J = +1/2 sublevel of the next highest energy subshell (5p). The laser is tuned to the wavelength required to match the energy difference between 5s and 5p. For Rb, this wavelength is 794.7nm (79). The excited electrons of the Rb nuclei then spontaneously return to the 5s subshell, populating the m_s = +½ sublevel and establishing greater electronic polarization. In returning to the ground state, fluorescent light is emitted to balance the change in energy between levels. This emitted energy can redistribute the ground state electrons between the two sublevels, effectively destroying the polarization. To limit this, an inert quenching gas such as N_2 is present in the cell to absorb the fluorescent energy. Polarization is also lost due to collisions between Rb molecules and Rb molecules and the cell wall. This causes electrons in the 5p subshell to distribute between the two spin sublevels. The polarization of Rb as a function of position along the long axis of the cell is given by (80):

$$P_{Rb}(z) = \frac{\gamma_{op}(z)}{\gamma_{op}(z) + \gamma_{sd}} \qquad [1.6.2]$$

; where $\gamma_{op}(z)$ is the optical pumping rate per atom of Rb and γ_{sd} is the spin destruction rate of Rb. The laser source is located at z = 0. The spin destruction rate is given by (79):

$$\gamma_{sd} = \Sigma_i \kappa_i n_i + \gamma_{se} + \gamma_{trap} \qquad [1.6.3]$$

; where κ_i is the binary collision coefficient of the i-th molecular species, n_i is the number density of the i-th species, γ_{se} is the spin-exchange rate (the rate at which the spin state of the Rb atom is transferred to an atom of the target gas to be hyperpolarized), and γ_{trap} is the rate of spin destruction due to fluorescence from excited electrons (this form of spin destruction is known as radiation trapping) (79). The optical pumping rate is given by (81):

$$\gamma_{op} = \int \Phi_{op}(\lambda)\sigma_{op}(\lambda)d\lambda \quad [1.6.4]$$

; where $\Phi_{op}(\lambda)$ is the photon flux as a function of wavelength and $\sigma_{op}(\lambda)$ is the Rb optical cross-section as a function of wavelength. Maximizing the optical pumping rate maximizes the polarization. Utilizing a high-power narrow-band laser achieves this by increasing the photon flux rate; however, this is potentially a costly solution, as more powerful lasers tend to be more expensive. A cheaper method is to increase the absorption spectrum of Rb to capture a broader range of wavelengths generated by the laser, thus making the optical pumping process more efficient. This can be achieved via pressure broadening through the introduction of ^{4}He gas into the cell. The increase in the linewidth of the Rb absorption profile is proportional to the density of ^{4}He in the gas mixture and is a function of temperature (82).

The polarized Rb transfers its angular momentum to other particles via binary collisions and the formation of van der Waals molecules, which are short-lived molecules held together by weak intermolecular forces between dipoles (83). Spin exchange via van der Waals molecule formation is the dominant interaction through which Rb and ^{129}Xe transfer spins. Random molecular collisions after spin exchange can hinder the build-up of ^{129}Xe polarization, therefore a low pressure within the pump cell is desirable (84). One must consider the trade-off with Rb absorption spectrum broadening when deciding the gas pressure within the cell.

Once a sufficient volume of ^{129}Xe has been hyperpolarized and collected, it must be used in a timely manner because the polarization spontaneously decreases to thermal equilibrium due to T_1 relaxation effects. These relaxation mechanisms may be intrinsic, such as the creation of Xe_2 dimers (85), or extrinsic, such as diffusion through the magnetic field of an MRI system (86). A dominant source of ^{129}Xe T_1 relaxation is interactions with O_2, which is why it is important that bags used for ^{129}Xe collection are vacuum-sealed and not contaminated by O_2. This is discussed further in § 1.7.2.1. To preserve the polarization of HP ^{129}Xe between its collection and its usage, it can be frozen by surrounding it with a bath of liquid N_2 (the freezing point of Xe is higher than N_2 and He). Surrounded by liquid N_2 at a temperature of 77 K, solid state naturally-abundant xenon has a T_1 of approximately 2.5 hours (87).

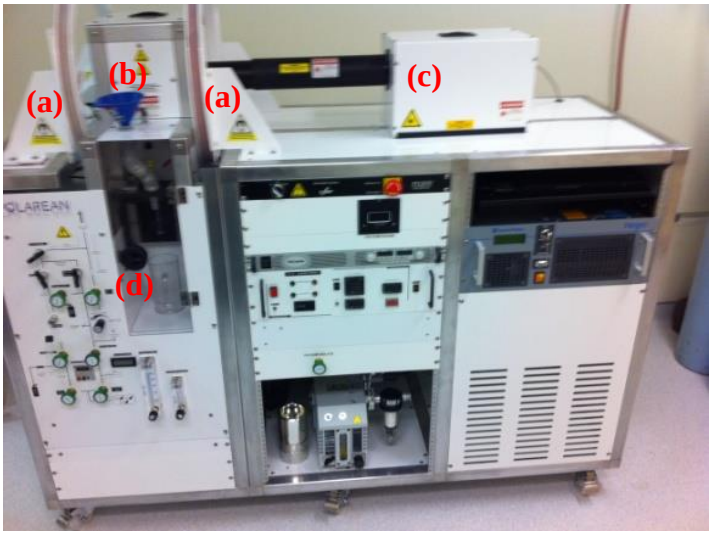

Figure 1.10: Polarizer for ^{129}Xe SEOP (Polarean, Durham, NC, USA) used at The Hospital for Sick Children, Toronto, Canada. (**a**) Helmholtz coils to induce Zeeman splitting of the Rb atoms. (**b**) Rubidium cell. (**c**) 794.7 nm wavelength circularly-polarized laser. (**d**) Collection cell (enclosed: cold finger for the accumulation of HP ^{129}Xe).

1.7 Multiple Breath Wash-Out Imaging

1.7.1 Overview

With HP ^{129}Xe MRI, lung ventilation can be directly imaged and lung function can be regionally assessed. However, a single snapshot of ventilation provides limited information. Measurements based on the absence of HP ^{129}Xe signal, such as VDP, can suggest where total airway obstructions or collapses may have occurred. However, these measurements are signal strength-dependent, and signal strength is affected by factors independent of ventilation such as gas polarization, RF coil and choice of RF pulse sequence. A series of "static" ventilation images showing signal evolution due to lung function may therefore be more informative since function would be dependent on relative signal changes rather than absolute signal. The per-breath rate of signal evolution may then be quantified to compare loss of function between regions, where function is defined by the rate of tracer gas wash-in or wash-out. Multiple breath imaging using HP gas MRI was first demonstrated by Deninger et al. in 2002 (88). First performed on mechanically ventilated guinea pigs using HP ^{3}He, the technique consisted of multiple cycles (M) of a constant number of air breaths followed by a variable number of ^{3}He pre-breaths (m), where m increases by one each cycle. At the final ^{3}He breath per cycle, a static ventilation image was acquired upon breath-hold. M static ventilation images were thus acquired, with each subsequent

image containing a greater volume of ^{3}He dependent on the tidal volume (*TV*). A signal equation was fit on a per-voxel basis to the series of images to acquire a map of lung function. Lung function in this study was defined as fractional ventilation (*r*) (89,90). *r* is a unitless parameter ranging from zero to one, where zero indicates no gas turnover and one indicates full replacement of old tracer gas with new gas. It is defined as the volume of fresh tracer gas (V_{fresh}) to the volume of total tracer gas at peak inspiration ($V_{total} = V_{fresh} + V_{residual}$) per breath per unit volume:

$$r = \frac{V_{fresh}}{V_{fresh} + V_{residual}}. \quad [1.7.1]$$

This method for multiple breath wash-in imaging has several drawbacks. Firstly, it requires a large volume of HP gas due to its multi-cycle scheme. This was addressed by the development of a wash-in imaging scheme in which images were acquired after each inhalation of ^{3}He and RF pulse flip angle was gradually increased to preserve signal (91). Secondly, the accumulated gas experiences unequal depolarization during wash-in due to gas exchange with the dead space of the ventilator and unequal exposure to the O_2-rich environment of the lungs (discussed further in § 1.7.2.1). This was addressed by incorporating modifications to theory that accounted for ventilator dead space volume (92).

Despite these improvements, there are further limitations to multiple breath wash-in imaging. It does not capture abnormal retention of gas in the lungs due to obstruction or reduced function, otherwise known as gas trapping. While it is present in all lungs, it is enhanced in CF patients due to symptoms such as airway infection and mucous plugging (5). Wash-in imaging also causes a decrease in blood oxygenation due to the repeated inhalation of an anoxic gas, which may be harmful. A normoxic gas mixture may be used, but this increases the rate of T_1 relaxation, thereby depleting available signal (§ 1.7.2.1) (93). Multiple breath wash-out (MBW) imaging, first demonstrated in humans by Horn et al. in 2014, is a viable alternative to wash-in imaging. In MBW imaging, the subject inhales the total provided volume of tracer gas and the distribution of gas is imaged during a breath-hold at peak inspiration. The subject then exhales and inhales, exchanging the gas in their lungs with room air. Another image is acquired during a breath-hold at peak inspiration, and the process is repeated for several air wash-out breaths of equal tidal volume (Fig. 1.11) (94). This generates a series of ventilation images that describes gas wash-out as a function of breath number. As with the Deninger model, an equation for signal evolution is fit

to the data on a per-voxel basis to extract a regional measurement of fractional ventilation. Whereas the wash-in model is dependent on r, wash-out is dependent on its complement, $1 - r$. Advantages of wash-out over wash-in imaging include: (i) the elimination of device dead space with which gas is exchanged between images, (ii) the absence of an anoxic multiple breath wash-in phase, and (iii) the ability to observe gas trapping.

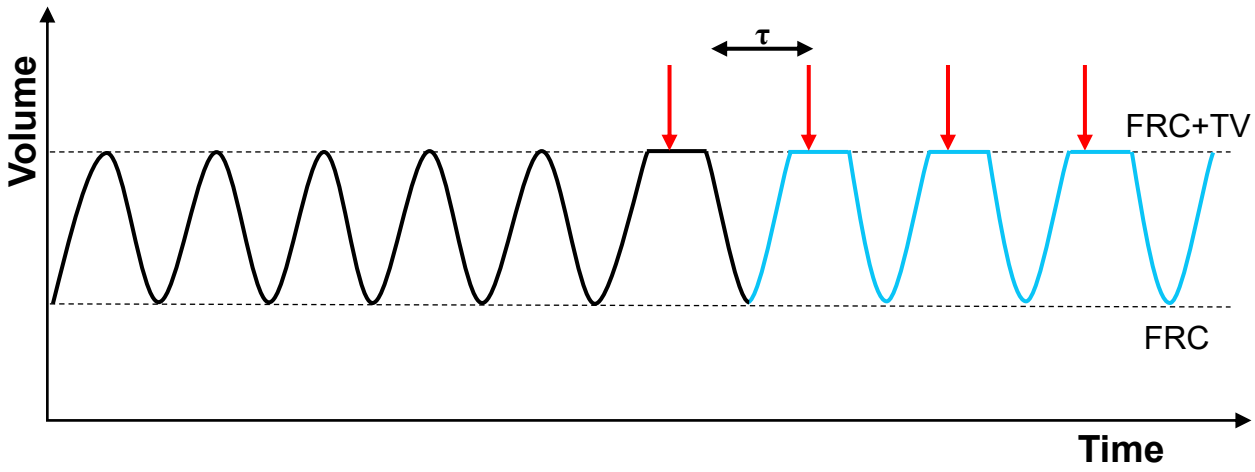

Figure 1.11: Schematic of HP ^{129}Xe MBW ventilation and imaging. Black lines indicate ^{129}Xe breaths and blue lines indicate air breaths. Arrows indicate the beginning of image acquisition. τ indicates inter-image delay, defined as the time between the end of a breath-hold and the beginning of the subsequent image acquisition. FRC represents functional residual capacity and TV represents tidal volume.

1.7.2 Confounding Sources of Signal Loss in MBW Imaging

In MBW imaging, several sources of signal loss independent of gas wash-out must be properly accounted for. As briefly discussed in § 1.5.2.1, hyperpolarization of ^{129}Xe is not recoverable once excited by the RF pulse, $\boldsymbol{B}_1(t)$. When the bulk magnetization $\boldsymbol{M}$ returns to the longitudinal direction due to T_1 relaxation, the polarization of the spin ensemble will return to thermal equilibrium ($P \sim 0$). RF pulse history (i.e., the number of pulses applied and their respective flip angles) must therefore be accurately known to properly account for signal loss due to RF depolarization. This requires measurement of the RF pulse flip angle as well as the mapping of B_1 inhomogeneity across the FOV. If accurate mapping cannot be performed, then inhomogeneity must be small (< 3%) in order to avoid significant error propagation when fitting the model to the signal data for extraction of r (95). To calibrate flip angle, one may use a series

of identical pulses to deplete the signal in a sample of HP ^{129}Xe and fit the data with an appropriate signal equation to extract flip angle (96). To make optimal use of the non-renewable signal, a low flip angle is used so that signal is deposited approximately uniformly throughout k-space. If the flip angle is too large, then the signal may be completely depleted before the imaging sequence has performed all the phase-encoding steps, leading to image blurring. Lines in k-space may be acquired in a pattern that maximizes signal in the centre of k-space while minimizing signal at the extremities. This ensures that high-contrast low spatial frequency information, such as coarse features, are captured at the cost of high spatial frequency information such as fine details and edge definition. One such pattern is a centric phase-encoding trajectory, which captures $k_y = 0$ first then alternately captures the next negative and positive lines of k-space, finishing by capturing the extremities of k-space. When a constant flip angle (CFA) approach is used, the optimal angle for a centric phase-encoding trajectory is given by:

$$\alpha = \tan^{-1}\left(\frac{1}{\sqrt{N-1}}\right) \qquad [1.7.2]$$

; where *N* is the total number of phase-encoding steps (96). More advanced imaging methods may use a variable flip angle (VFA) approach, which utilizes an optimal trajectory of flip angles that increases from its lowest value to 90^o over the course of traversing k-space (91). This ensures that signal is distributed equally throughout k-space. The disadvantage of this is that the signal per line of k-space will be lower than the maximum signal acquired by a CFA approach using the optimal flip angle. A more recent study has investigated a hybrid CFA-VFA approach, which optimizes the trade-off between maximizing signal per RF pulse with equally distributing signal throughout k-space (97).

Another source of signal loss unrelated to HP ^{129}Xe wash-out is uptake of HP ^{129}Xe into the bloodstream and tissues. When ^{129}Xe is not in a gaseous environment but instead dissolved in blood or tissue, its resonant frequency experiences a chemical shift as given by Eq. 1.6.1. When ^{129}Xe dissolves in tissue, plasma, or blood, its shifted resonant frequency is typically beyond the bandwidths used for gas phase imaging and is thus not detected. Therefore dynamic exchange with dissolved ^{129}Xe causes some signal loss from the gas phase (98). The amount of ^{129}Xe transfer between the gas and dissolved phase can be measured using imaging techniques that either measure the dissolved signal directly (99) or indirectly (100). It has been shown that when

saturated, the dissolved ^{129}Xe signal from the parenchyma is only approximately 2% that of the gas signal (100). Because this is a reasonably small amount of signal loss compared to wash-out via tidal breathing, ^{129}Xe uptake is generally ignored in wash-out and wash-in imaging studies (74,101) and will be likewise ignored in the study presented in this thesis.

1.7.2.1 T_1 Relaxation of Hyperpolarized ^{129}Xe

The major confounding source of signal loss – and the focus of this thesis – is T_1 relaxation. As described in § 1.4.2.1, T_1 relaxation is due to spin-exchange interactions between the HP ^{129}Xe nuclei and the magnetic dipoles within its environment. The dominant source of T_1 relaxation of ^{129}Xe gas in the lungs is spin-exchange interactions with molecular O_2, which is paramagnetic due to unpaired electrons found within its molecular bonding orbitals. ^{129}Xe and O_2 induce mutual spin flips and over time, the polarization of ^{129}Xe returns to thermal equilibrium and hyperpolarization is lost (102). O_2-induced T_1 relaxation in vitro is approximately given by:

$$T_1 = \frac{\zeta}{pO_2} \qquad [1.7.3]$$

; where ζ is the oxygen enhancement factor and pO_2 is the partial pressure of O_2 (84). O_2-induced T_1 relaxation is also dependent on temperature and Larmor frequency, but the effect of these factors on T_1 is small relative to pO_2. Note that this relationship was established in vitro and as such may not accurately account for all T_1 relaxation mechanisms in the context of HP gas MRI of the lungs, where additional mechanisms such as interactions between ^{129}Xe and the tissue and diffusion through magnetic field gradients may need to be considered (86). To measure T_1 in the lungs, one approach is to acquire a pair of HP ^{129}Xe lung images during a breath-hold and fit the signal equation (96) to the data, provided that flip angle is accurately known. T_1 of ^{129}Xe in the lung is expected to be roughly 20 s (84). MBW imaging in humans may take roughly 30 s to perform or longer if higher resolution images or longer inter-image delay times are used (101). For $T_1 \sim 20$ s and $t \sim 30$ s, $e^{-\frac{t}{T_1}} \approx 0.22$; therefore, an estimated 78% loss of the originally available signal over the duration of MBW imaging is expected due to T_1 signal decay.

The Horn et al. method of MBW imaging (§ 1.7.1) involves a calibration phase during an extended breath-hold immediately before wash-out. By acquiring two images during that initial breath-hold, RF depolarization and T_1 relaxation are measured simultaneously. In making these

measurements, the Horn work makes two assumptions: (i) ^{129}Xe uptake is a negligible source of signal loss and can reasonably be ignored, and (ii) T_1 is constant throughout wash-out. The former is justified in § 1.7.2. The latter is at odds with what is expected due to the changing gas composition within the lungs during wash-out. As ^{129}Xe is being replaced by room air, the alveolar partial pressure of O_2 (p_AO_2) of the lungs will increase. Due to the strong dependence of T_1 on p_AO_2 (Eq. 1.7.3), T_1 is expected to decrease as a function of wash-out breath. That is, T_1 relaxation becomes an increasingly significant source of signal loss as wash-out progresses. Unfortunately, explicitly measuring T_1 as a function of wash-out breath ($T_1(n)$) during MBW imaging would require longer breath-holds (roughly 10 s each (94)), which may not be feasible for CF patients. It would also cause a greater loss in signal due to additional RF depolarization and additional T_1 relaxation.

1.7.3 Hypothesis

While multiple breath imaging using HP gas MRI is a technique with a 14-year research history (88), the use of ^{129}Xe as the tracer gas is fairly new and the development of wash-out techniques has largely occurred within the last few years (93,94) (only one paper has been published to date that explores MBW imaging using HP ^{129}Xe MRI (101)). Given its short and recent history, the effect of $T_1(n)$ on MBW imaging using HP ^{129}Xe has yet to be explored. This thesis investigates the hypothesis that failing to account for how T_1 changes over the course of MBW imaging leads to an over-estimation of fractional ventilation. This over-estimation of fractional ventilation may be accounted for using a MBW imaging model of $T_1(n)$. An experimental study in healthy mechanically-ventilated rats is conducted to investigate this bias. The effects of timescale and tidal volume on the measurement of r using a constant T_1 model and a model of $T_1(n)$ are explored.

The contents of chapter 2 were originally presented in a manuscript entitled “Effect of T_1 Relaxation on Ventilation Mapping Using Hyperpolarized ^{129}Xe Multiple Breath Wash-out Imaging” submitted to the journal *Magnetic Resonance in Medicine*. The co-authors of this paper are Felipe Morgado, Marcus J. Couch, Elaine Stirrat, and Giles Santyr. Marcus J. Couch assisted with experiment design found under the subheading “MRI” as well as MRI system operation and pulse sequence development. Elaine Stirrat assisted with experiment design found under the subheading “Animal Preparation” as well as rat intubation, anesthetization and disposal. Dr. Giles

Santyr assisted with experiment design, data analysis and interpretation. Felipe Morgado led the experimental design, data acquisition, data analysis and interpretation. The manuscript, figures, and tables were prepared by Felipe Morgado. All co-authors assisted with the editing of the manuscript.

Chapter 3 discusses the presented work in further detail, including the limitations of this study and necessary considerations for clinical translation. Recommendations for next steps are given.

Chapter 2

2 Effect of T_1 Evolution on Ventilation Mapping using Hyperpolarized ^{129}Xe Multiple Breath Wash-out Imaging

2.1 Introduction

Hyperpolarized (HP) gas MRI has been demonstrated as a safe and effective approach for regional measurement of lung function in humans and animals, providing novel insight into the spatial heterogeneity of ventilation in obstructive diseases, such as asthma and cystic fibrosis (50,103). HP gas MRI typically acquires a single multi-slice data set following a single breath-hold of HP gas, providing a static "snap shot" of the spatial distribution of the gas at one point in time. However, this approach is sensitive to the total HP gas signal, which can vary depending on instrumental parameters such as polarization level, RF coil, etc. Furthermore, this only measures lung ventilation within a single breath and thus does not capture phenomena such as late-filling defects and air trapping and associated rate constants. This has in part inspired the development of multiple breath HP gas MRI techniques, which utilize the signal intensity changes as a function of breath number to regionally assess air trapping (104) as well as quantify gas wash-out and wash-in rates (93,94).

As discussed in § 1.7.1, multiple breath HP gas MRI was first developed in 2002 by Deninger et al. (88). In this study, fractional ventilation, *r* (Eq. 1.7.1), was mapped during multiple-breath wash-in of HP ^{3}He gas in guinea pigs. Since the Deninger et al. study, significant improvements in the speed and efficiency of the technique have been demonstrated in rodents (91,105). Clinical wash-out imaging approaches have also since been developed to measure *r*, in which the subject exhales the HP gas over a series of wash-out breaths after an initial HP gas inhalation (94). Advantages of multiple breath wash-out (MBW) imaging compared to wash-in techniques include: (i) no exchange of fresh HP gas with previously exhaled gas within instrument dead space (92), and (ii) a greater sensitivity to gas trapping (104). Mapping of *r* by MBW imaging in humans was originally studied by Horn et al. using HP ^{3}He (94) and has more recently been performed using HP ^{129}Xe (101). Advantages of using ^{129}Xe instead of ^{3}He include a relatively high natural abundance and lower cost (50,74).

To account for sources of signal loss unrelated to gas wash-out in HP gas MRI, correction for the effect of RF-induced depolarization and T_1 relaxation on MBW signal decay is necessary. While RF-induced depolarization can be corrected for by suitable flip-angle mapping, the rate of T_1 relaxation is proportional to the partial pressure of O_2 within the lungs (p_AO_2) and depends on physiology (102). As HP gas is washed out of the lungs during MBW imaging, it is replaced with air, thereby increasing the p_AO_2 with each breath and consequently decreasing T_1. Explicitly mapping T_1 after each wash-out breath would quickly deplete the limited signal available and require longer breath-holds, which may be difficult for a patient to perform. In the work of Horn et al., the combined effect of both flip angle and T_1 was corrected for with a calibration phase and was assumed to be constant throughout the MBW manoeuver (94,101). However, assuming T_1 remains a constant value measured at the outset of MBW is expected to underestimate ^{129}Xe concentration in later breaths due to increasing p_AO_2, leading to an over-estimation of r. O_2-induced T_1 relaxation in HP gas MRI has been thoroughly investigated for ^{3}He ventilation imaging (95,106,107). However, few studies have investigated this for HP ^{129}Xe (108,109), and the dependence of HP ^{129}Xe T_1 on wash-out breath number, $T_1(n)$, has yet to be investigated.

The purpose of this work was to model and experimentally validate the effect of $T_1(n)$ on estimation of r in healthy mechanically-ventilated rats using HP ^{129}Xe MBW imaging. The dependence of T_1 on breath number was modelled based on previously published work (106) and verified experimentally by explicitly measuring $T_1(n)$ for $0 \leq n \leq 2$ in a subset of the rat cohort. The effect of $T_1(n)$ on the r measurement bias was investigated for different inter-breath times and tidal volumes. The application of this approach in the clinical setting and the implications of this bias on the mapping of fractional ventilation in disease are discussed.

2.2 Methods

2.2.1 Theory

p_AO_2-induced T_1 as a function of breath number was determined using the equations:

$$T_1(n) = \frac{\zeta}{p_AO_2(n)}; \qquad [2.1]$$

$$p_AO_2(n) = (1 - r) \cdot p_AO_2(n - 1) + r \cdot (p_IO_2 - R \cdot \Delta). \quad [2.2]$$

Equation 2.1 is based on in vitro O_2-induced ^{129}Xe T_1 relaxation measurements by Jameson et al. (84,102). Equation 2.2 is adapted from Eq. 17 from Möller et al. (106) and Eq. 3 from Hamedani et al. (93). In Eq. 2.1, ζ is the oxygen-enhancement factor (102). $\zeta = 2.68$ bar·s for ^{129}Xe imaged at 3.0 T and 295 K (84,92,102). In Eq. 2.2, p_IO_2 is the inspiratory partial pressure of O_2, R is the apparent O_2 uptake rate constant and Δ is the time between the start of two consecutive image acquisitions in MBW imaging (i.e., image acquisition time plus time between breath-holds). This study assumes that O_2-induced T_1 relaxation is the dominant source of HP gas T_1 relaxation in the lungs and thus ignores other T_1 relaxation mechanisms, such as surface interactions and gradient field effects (86).

$T_1(n)$ was applied to the signal equation for a gradient-recalled echo imaging sequence (GRE) with centric-ordered phase encoding and a constant flip angle (94,110):

$$S(n) = S_0 \cdot \sin\alpha \cdot \left[\cos^{N_y}\alpha \cdot e^{-\left(\frac{N_y \cdot TR + \tau}{T_1(n)}\right)} \cdot (1 - r)\right]^n, \quad [2.3]$$

where α is the flip angle, N_y is the number of phase-encoding steps, and τ is the inter-image delay time (i.e., the time between the end of one breath-hold and the beginning of the subsequent image acquisition). The $(1 - r)$ factor accounts for gas wash-out by ventilation. Signal loss due to ^{129}Xe uptake into the lung parenchyma and bloodstream was ignored since it is considered to be negligible relative to signal loss due to gas wash-out (100,111). Eq. 2.3 also assumes that T_2^* is constant for all n. T_2^* contributions from p_AO_2, which increases with n, are much smaller than T_2^* contributions due to the large magnetic susceptibility difference between the lung tissue and the gas space (112). In a previous study of ^{129}Xe T_2^* in the gas phase measured in rats imaged at 3.0 T, mean T_2^* was 8 ms (113).

Eqs. 2.1 – 2.3 were used to determine r. To determine the signal bias incurred by assuming a constant T_1 (94) compared to explicitly including $T_1(n)$, Eq. 2.3 was modified by fixing $T_1(n)$ to equal $T_1(0)$ for all n and by replacing r with the free parameter r'. Therefore r' represented the biased estimate of r incurred by assuming a constant T_1 during MBW. The amount by which r' overestimated r was expressed as the percent relative bias:

$$\Delta r\ (\%) = \frac{r' - r}{r} \times 100\% \qquad [2.4]$$

2.2.2 Experiment

2.2.2.1 Animal Preparation and Ventilation

All procedures followed an animal use protocol approved by The Hospital for Sick Children's Animal Care Committee and were consistent with guidelines provided by the Canadian Council on Animal Care. Eight healthy Sprague-Dawley rats (mass = 446 g ± 24 g) (Charles River Laboratories, Saint-Constant, Canada) were prepared as previously described (91). Briefly, the rats were anesthetized by intravenous administration of a 10:1 mixture of propofol and ketamine at a rate of ~45–60 mg/kg/h and a tracheotomy was performed. The rats were mechanically-ventilated in the supine position using a custom MRI- and HP gas-compatible ventilator (GEHC, Malmö, Sweden) (91) (Figs. 2.1 and 2.2). When ventilating with medical grade air between scans, the respiratory rate of the rats was 60 breaths per minute and provided at a tidal volume (*TV*) of 8 mL/kg (V_{dose}). *TV* was calibrated for a peak inspiratory pressure of approximately 12 cm H_2O. There exists a small dead space volume between the rat and the expiratory valve, potentially allowing for some re-breathing of previously exhaled gas. This dead space volume was assumed to be negligible relative to the rats' tidal volumes. Furthermore, the absence of a positive end-expiratory pressure meant that exhalation occurred in an uncontrolled and rapid fashion. While this did not accurately reflect natural respiration, it assisted with clearing the dead space volume during each exhalation.

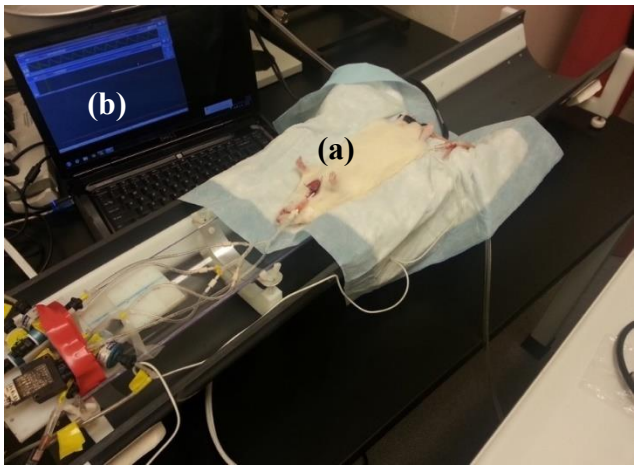

Figure 2.1: Mechanically-ventilated Sprague-Dawley rat. The rat was anesthetized with a 10:1 mixture of propofol and ketamine at a rate of ~45–60 mg/kg/h. Medical grade air and HP ^{129}Xe was supplied through a catheter inserted via a tracheotomy (**a**). Gas supply was controlled using pneumatic valves controlled by customized software (LabVIEW®, National Instruments, Austin, TX) (**b**) (91).

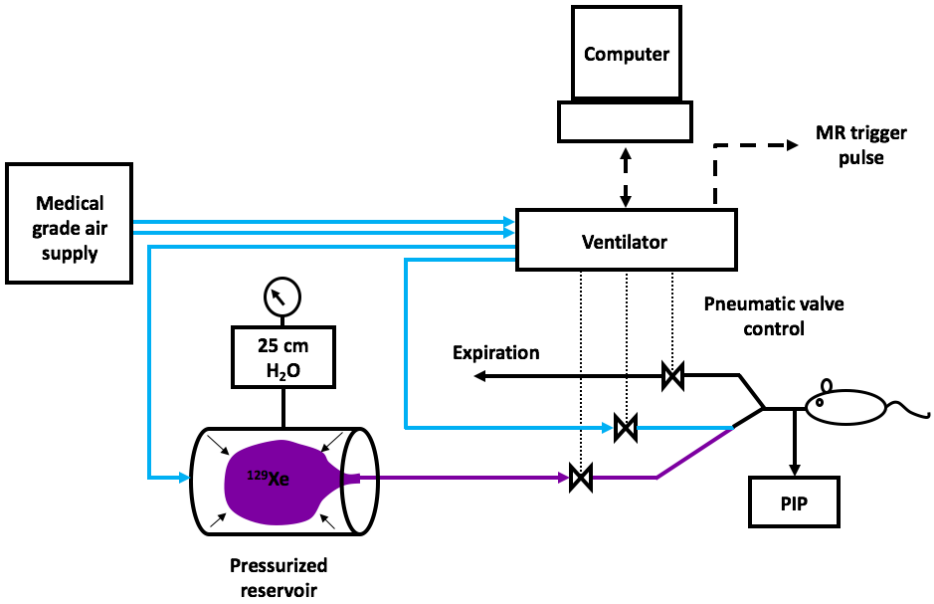

Figure 2.2: Diagram of the custom MRI- and HP-gas compatible rat ventilator (GEHC, Malmö, Sweden). Blue lines indicate medical grade air and purple lines indicate HP ^{129}Xe. The tidal volume of the rat was calibrated for a peak inspiratory pressure (PIP) of approximately 12 cm H_2O.

For T_1 mapping, the rats were first given five breaths of 100% HP ^{129}Xe at a rate of 30 breaths per minute at $TV = V_{dose}$ followed by an 11 s breath-hold at peak inspiration (Fig. 2.3). For MBW imaging, the rats were also given five breaths of 100% HP ^{129}Xe at a rate of 30 breaths per minute at $TV = V_{dose}$. This was followed by the wash-out phase which consisted of four sets of

breath-holds and air wash-out breaths. Images were acquired during breath-holds at peak inspiration. To measure the effect of duration and lung function on the measurement of r and r', τ and TV during wash-out were manipulated. The following combinations of τ and TV were examined, where TV refers to the tidal volume of the wash-out breaths: $\tau = 2$ s, $TV = V_{dose}$; $\tau = 4$ s, $TV = V_{dose}$; $\tau = 6$ s, $TV = V_{dose}$; $\tau = 4$ s, $TV = V_{dose} - 1$ mL; and $\tau = 4$ s, $TV = V_{dose} + 1$ mL. The delay defined by τ was provided by extending the breath-holds during wash-out. This range of τ was chosen to investigate T_1 signal loss for increasingly longer MBW imaging schemes, mimicking the additional time required to acquire higher-resolution images (e.g. 3D compared to 2D imaging). TV was changed by ± 1 mL because this is roughly equivalent to a ± 10% change in lung volume at peak inspiration. Lung volume, defined here to be the sum of functional residual capacity and tidal volume, is roughly 10 mL for rats of similar weight to the ones in this study (74). This % change reflects the variation in TV expected in human MBW imaging for which TV regulation is effort-dependent (94).

At the end of the experiment, the animals were euthanized using sodium pentobarbital (150 mg/kg) (Euthanyl Forte, Bimeda-MTC, Cambridge, Canada).

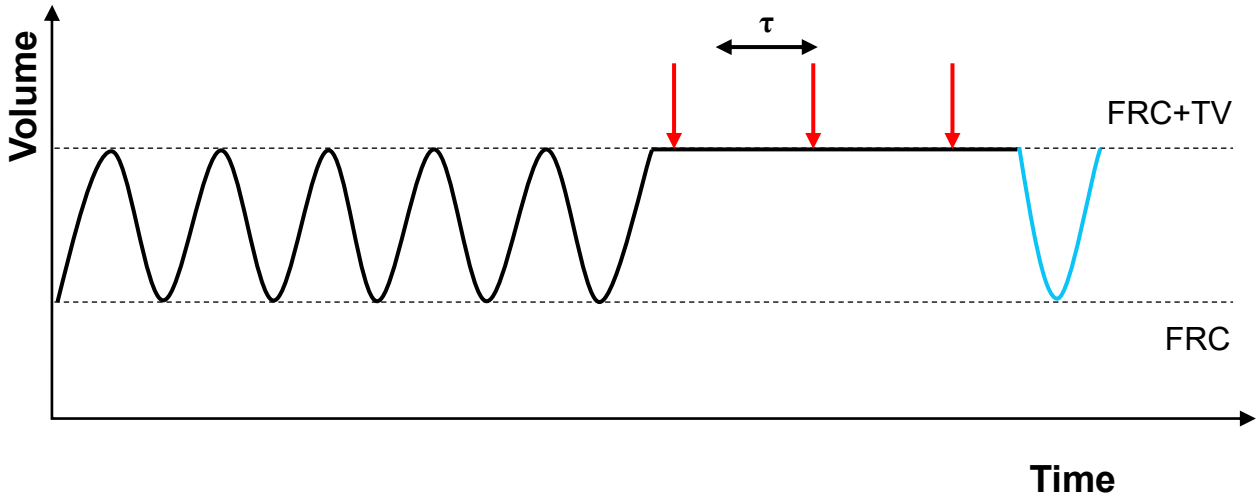

Figure 2.3: Schematic of T_1 mapping ventilation and imaging. Black lines indicate ^{129}Xe breaths and blue lines indicate air breaths. Arrows indicate the beginning of image acquisition. τ indicates inter-image delay, defined as the time between the end of an image acquisition and the beginning of the subsequent image acquisition. FRC represents functional residual capacity and TV represents tidal volume.

2.2.2.2 MRI

MRI was performed at 3.0 T (Siemens MAGNETOM Prisma, Siemens AG, Munich Germany) using a transmit-receive birdcage coil with an inner diameter of 15 cm tuned to 34.09 MHz (Morris Instruments, Ottawa, Canada). To hyperpolarize ^{129}Xe gas, spin-exchange optical pumping was performed using a continuous-flow polarizer (Polarean 9800, Polarean Inc., Durham, NC). Enriched xenon gas (85% ^{129}Xe) was supplied to the polarizer in a gas mixture containing N_2 and He (114). ^{129}Xe was polarized to approximately 15% polarization at a rate of 15 mL/min and collected in 300 mL batches in Tedlar® bags (Chromatographic Specialties Inc., Brockville, Canada).

Single-slice coronal projection images were acquired using a 2D GRE sequence with centric-ordered phase encoding ($\alpha = 4^o$, TR = 13.0 ms, TE = 3.33 ms, FOV = 7 cm x 7 cm, BW = 100 Hz/Px, $N_x = 40$, $N_y = 64$ and 62.5% partial echo acquisition). The FOV was centred on the rat thorax. Flip angle was calibrated prior to imaging each rat by acquiring signals from the lungs after three pre-breaths of ^{129}Xe with no phase-encoding. A whole-lung measurement of flip angle was used as it has been previously shown that a rigid transmit/receive bird-cage coil of the same size as the one used in this study provides sufficiently homogeneous B_1 to provide reliable T_1 estimates (95). For T_1 mapping, three images separated by 3 s intervals were acquired during breath-hold prior to wash-out (i.e., $n = 0$). In a subset of the rats (rats 1, 3, 4, and 5), T_1 mapping was also performed at $n = 1$ and $n = 2$ to validate the $T_1(n)$ trajectory predicted by Eqs. 2.1 and 2.2. For MBW imaging, one image per breath-hold was acquired for a total of four images at four separate breath-holds.

Coronal projection images were acquired to increase the SNR of the images; however, this meant that voxels in the *r* maps reflected average ventilation along the anterior-to-posterior (A/P) direction. It is known that a ventilation gradient is present in this direction when the subject is supine (11,115). To validate the presence of this gradient, additional MBW imaging was performed with axial projection images in rat 7 ($\tau = 4$ s, $TV = V_{dose}$). The slopes of 10 profiles along the A/P direction of the axial *r* map were measured and averaged. The averaged measurement was compared to previously published measurements from a similar HP ^{129}Xe imaging study in rats (74).

2.2.2.3 Data Analysis

MBW imaging and T_1 mapping were repeated twice to improve SNR by signal averaging. Averaging was performed prior to fitting Eq. 2.3 to the data. Image reconstruction was performed in Matlab® vR2013a (The Mathworks, Natick, MA), along with all image manipulation and model fitting for $T_1(n)$, R, r and r'. Raw k-space data were filtered using a Hamming window before zero-filling to a 64x64 matrix and performing an inverse Fourier transform. The images were corrected for background signal using $S' = \sqrt{S^2 - \sigma^2}$, where S is the signal and $\sigma = \bar{B}\sqrt{2/\pi}$, where $\bar{B}$ is mean background signal in a region of interest away from the lungs (116,117). SNR of the wash-out images was calculated by dividing mean signal in a region of interest in the right lung by the standard deviation of the signal in a region of interest in the image background away from the lungs. The images were segmented using a semi-automated seeded region-growing method. Major airways were masked to avoid conducting lung regions and the diaphragm region was masked due to its lower signal density in these coronal projections.

Baseline T_1 maps ($T_1(0)$) and R maps were acquired by per-voxel least-squares fitting a single breath version of Eq. 2.3 (r = 0) to the images acquired during the extended T_1 mapping breath-hold. Eq. 2.1 was modified to account for O_2 uptake; i.e., $T_1(0) = \zeta/(p_A O_2(0) - R \cdot \Delta)$. By mapping R during T_1 mapping as opposed to during MBW, R was de-coupled from r during the fit. For simplicity, R was assumed to be constant during wash-out. To determine whether $T_1(n)$ as modelled by Eqs. 2.1 and 2.2 agreed with the explicit measurements of $T_1(n)$ at n = 0, 1, and 2 in rats 1, 3, 4, and 5, mean measured $T_1(n)$ and mean predicted $T_1(n)$ were plotted. The slopes of the two trajectories, generated by linear regression, were tested for statistically significant difference using a two-tailed paired t-test. Linear regression and all statistical testing were performed in GraphPad® Prism 5 (GraphPad Software, Inc., La Jolla, CA).

Two sets of r maps were acquired by per-voxel least-squares fitting of Eqs. 2.1 – 2.3 to the MBW image signals. In the first case, T_1 was fixed to $T_1(0)$ to generate r' maps. In the second case, T_1 evolved as a function of wash-out breath according to Eqs. 2 and 3. Δr was calculated using Eq. 2.4 and the mean values of r and r'. To validate the measurements of r, r was also measured in a region of interest in the major airways, where its value was expected to be close to 1 due to near-complete gas wash-out in one breath. Bland-Altman plots of Δr as a function of mean r were generated from the data to determine mean Δr for each set of imaging and ventilation parameters.

Linear regression was performed on each plot and the slope was tested for a statistically significant difference from zero to analyze how bias changed as a function of *r*. Repeated measures one-way ANOVA tests followed by post-hoc pair-wise comparisons using Tukey's test were performed to determine whether changing τ or *TV* led to significantly different Δr. In addition to comparing the means of *r* and *r*' maps, changes in distribution (i.e., standard deviation and skewness) between the histograms derived from the maps were also tested for significant difference using a two-tailed paired t-test. The significance level for all tests was 0.05.

2.3 Results

Figure 2.4 shows the predicted $T_1(n)$ and the measured mean $T_1(n)$ in the subset of the rat cohort (n = 4). The model predicted $T_1(n)$ to within 1 standard deviation for all *n* when averaged over the four rats. Performing linear regression on the measured $T_1(n)$ and predicted $T_1(n)$ trajectories gave slopes that were not significantly different (-5.8 s·breath^{-1} and -7.0 s·breath^{-1}, respectively; P = 0.2556). Table 2.1 summarizes the $T_1(n)$ measurements for these four rats. For comparison, the time-course of the wash-out experiments ranged from approximately 9 s for τ = 2 s to approximately 21 s for τ = 6 s. Applying Eq. 2.1, $T_1(0)$ = 35 s is equivalent to a p_AO_2 of 57 mm Hg. The mean $T_1(2)$ of the rat subset was equal to 23 s and is equivalent to a p_AO_2 of 87 mm Hg (p_AO_2 in lungs filled with 100% air is approximately 100 mm Hg).

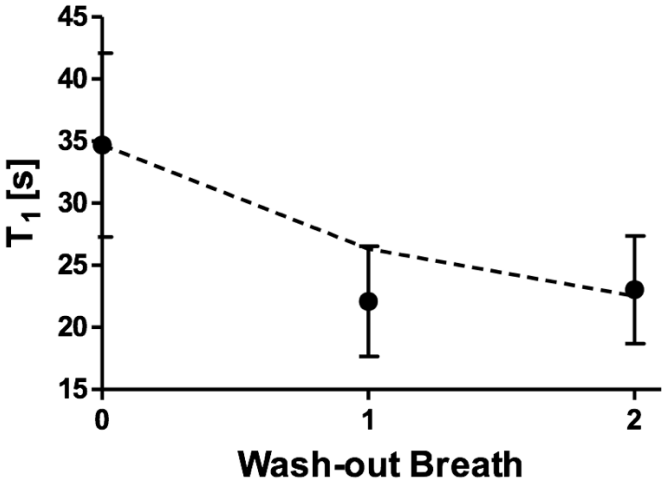

Figure 2.4: Measured mean $T_1(n)$ (symbols) compared to $T_1(n)$ predicted with Eqs. 2.1 and 2.2 (dotted line), averaged over the sub-set of rats 1, 3, 4, and 5 (mean ± SD). Linear regression of the measured $T_1(n)$ and predicted $T_1(n)$ trajectories produced slopes that were not significantly different (-5.8 s·breath^{-1} and -7.0 s·breath^{-1}, respectively; P = 0.2556).

Rat no.	$T_1(0)$ [s]	$T_1(1)$ [s]	$T_1(2)$ [s]
1	30 ± 3	20 ± 3	21 ± 3
3	35 ± 3	23 ± 3	24 ± 4
4	45 ± 6	28 ± 5	28 ± 5
5	29 ± 4	17 ± 3	18 ± 3
Grand mean	35 ± 7	22 ± 4	23 ± 4

Table 2.1: T_1 values (mean ± SD) for $0 \leq n \leq 2$ measured in the sub-set of rats 1, 3, 4, and 5.

Table 2.2 summarizes the findings for each rat, where mean and standard deviation of each *r* map, *r*' map, $T_1(0)$ map, and *R* map are provided. Grand mean *R* (*R* = 7.7 ± 2.0 mm Hg/s) was in good agreement with previously published values from a ^{3}He ventilation imaging study in rats (107). All the means of *r* maps were lower than the means of the respective *r*' maps, as expected. Figure 2.5 shows a representative set of wash-out images from rat 1 imaged at τ = 2 s and $TV = V_{dose}$ prior to segmentation and background removal. An SNR decrease of 85% was observed from n = 0 to n = 2. Figure 2.6 shows representative $T_1(0)$, *R*, *r*, and *r*' maps with the respective histograms, again from rat 1 imaged at τ = 2 s and $TV = V_{dose}$. The *r*' histogram demonstrated a non-linear positive bias relative to the *r* histogram.

				τ = 2 s, $TV = V_{dose}$		τ = 4 s, $TV = V_{dose}$		τ = 6 s, $TV = V_{dose}$		τ = 4 s, $TV = V_{dose}$ - 1 mL		τ = 4 s, $TV = V_{dose}$ + 1 mL	
Rat no.	**Mass [g]**	**$T_1(0)$ [s]**	**R [mm Hg/s]**	*r'*	*r*	*r'*	*r*	*r'*	*r*	*r'*	*r*	*r'*	*r*
1	450	30 ± 3	6.4 ± 1.9	0.35 ± 0.04	0.31 ± 0.04	0.36 ± 0.04	0.31 ± 0.04	0.40 ± 0.05	0.34 ± 0.05	0.36 ± 0.04	0.30 ± 0.04	0.39 ± 0.04	0.34 ± 0.04
2	450	65 ± 14	12.5 ± 1.2	0.40 ± 0.03	0.34 ± 0.03	0.44 ± 0.03	0.38 ± 0.03	0.49 ± 0.03	0.44 ± 0.03	0.39 ± 0.04	0.33 ± 0.04	0.44 ± 0.03	0.38 ± 0.03
3	410	35 ± 3	8.3 ± 1.6	0.36 ± 0.04	0.32 ± 0.04	0.38 ± 0.03	0.32 ± 0.03	0.40 ± 0.03	0.34 ± 0.03	0.33 ± 0.03	0.28 ± 0.03	0.38 ± 0.03	0.33 ± 0.03
4	410	45 ± 6	10.2 ± 1.5	0.30 ± 0.03	0.25 ± 0.03	0.34 ± 0.04	0.28 ± 0.03	0.38 ± 0.04	0.32 ± 0.04	0.30 ± 0.04	0.24 ± 0.03	0.34 ± 0.03	0.28 ± 0.03
5	450	29 ± 4	5.8 ± 2.5	0.39 ± 0.04	0.35 ± 0.04	0.42 ± 0.04	0.36 ± 0.04	0.43 ± 0.04	0.37 ± 0.05	0.38 ± 0.04	0.32 ± 0.04	0.44 ± 0.04	0.38 ± 0.04
6	475	26 ± 4	4.9 ± 2.9	0.34 ± 0.04	0.31 ± 0.04	0.36 ± 0.05	0.31 ± 0.04	0.37 ± 0.06	0.31 ± 0.06	0.33 ± 0.05	0.28 ± 0.05	0.38 ± 0.05	0.33 ± 0.05
7	470	33 ± 5	7.6 ± 2.5	0.34 ± 0.04	0.30 ± 0.04	0.37 ± 0.04	0.31 ± 0.04	0.39 ± 0.05	0.34 ± 0.05	0.35 ± 0.04	0.29 ± 0.04	0.36 ± 0.05	0.31 ± 0.05
8	450	46 ± 8	10.4 ± 1.8	0.27 ± 0.04	0.22 ± 0.04	0.29 ± 0.04	0.24 ± 0.04	0.32 ± 0.05	0.27 ± 0.05	0.28 ± 0.04	0.23 ± 0.03	0.31 ± 0.06	0.25 ± 0.06
Grand mean	446 ± 24	35 ± 7	7.7 ± 2.0	0.34 ± 0.04	0.30 ± 0.04	0.37 ± 0.04	0.31 ± 0.04	0.40 ± 0.05	0.34 ± 0.05	0.34 ± 0.04	0.28 ± 0.04	0.38 ± 0.04	0.33 ± 0.04

Table 2.2: Summary of *r*' and *r* (mean ± SD), $T_1(0)$ (mean ± SD), and *R* (mean ± SD) for all rats.

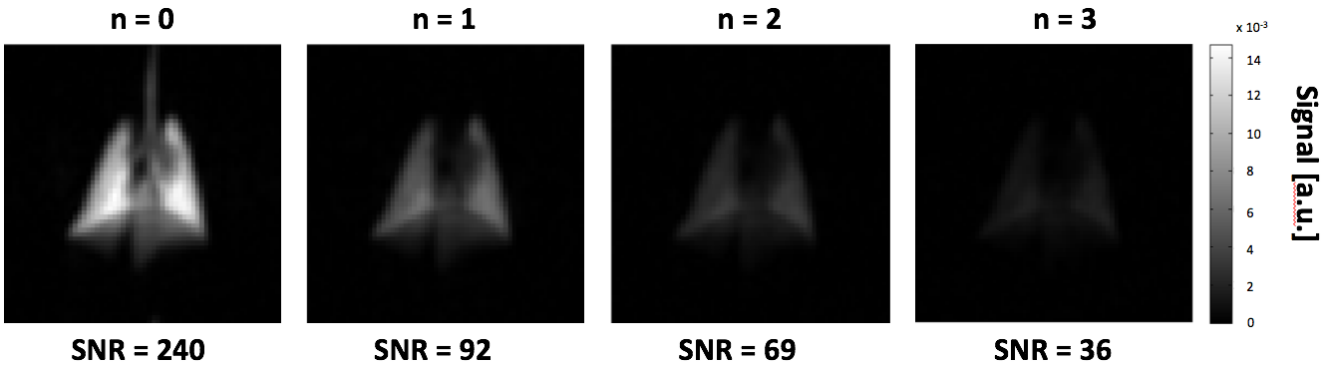

Figure 2.5: Representative ^{129}Xe wash-out trajectory acquired from rat 1 at τ = 2 s and $TV = V_{dose}$. Images shown and calculated SNR are prior to segmentation and background removal.

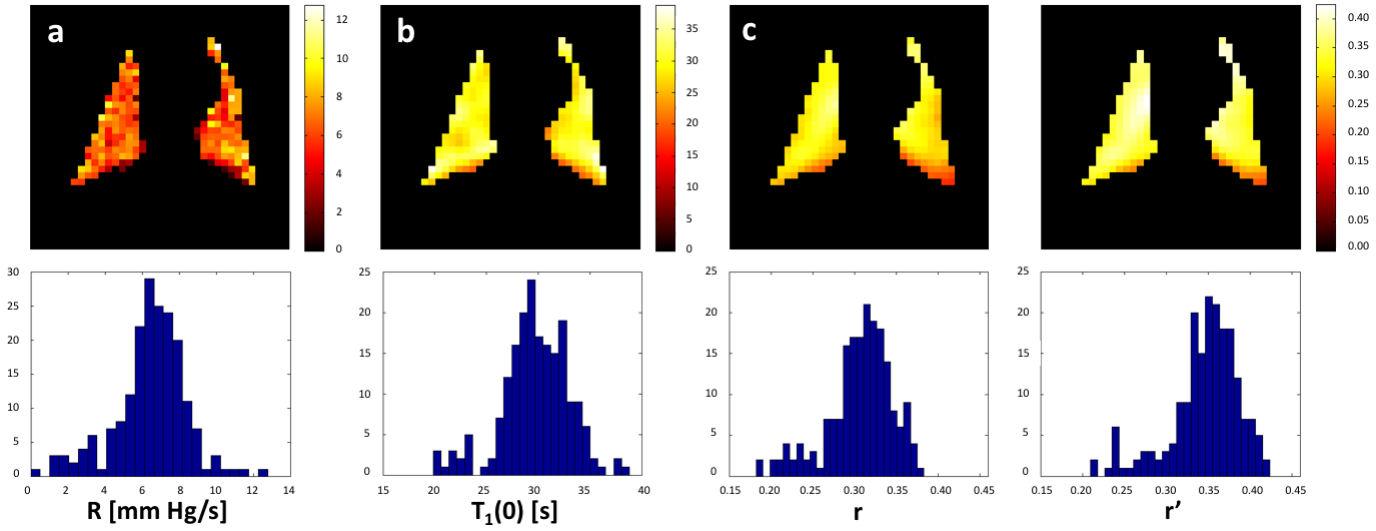

Figure 2.6: Representative (**a**) *R* map, (**b**) $T_1(0)$ map, (**c**) *r* map and (**d**) *r*' map and the respective histograms (below) acquired from rat 1 at τ = 2 s and $TV = V_{dose}$.

Figure 2.7 shows Δr as a function of mean *r* at the same wash-out *TV* (Fig. 2.7a) and the same duration (Fig. 2.7b), and Table 2.3 lists Δr for all combinations of τ and *TV*. Mean Δr as shown in Figs. 2.7a and 2.7b were 16.1% and 18.1%, respectively. The over-estimation of *r* incurred by fixing T_1 to $T_1(0)$ was the highest at reduced *TV* (Δr = 19.3%). In all cases, the slope of the best-fit line obtained by linear regression deviated significantly from zero and was negative. Therefore, the bias was the largest at lower *r*.

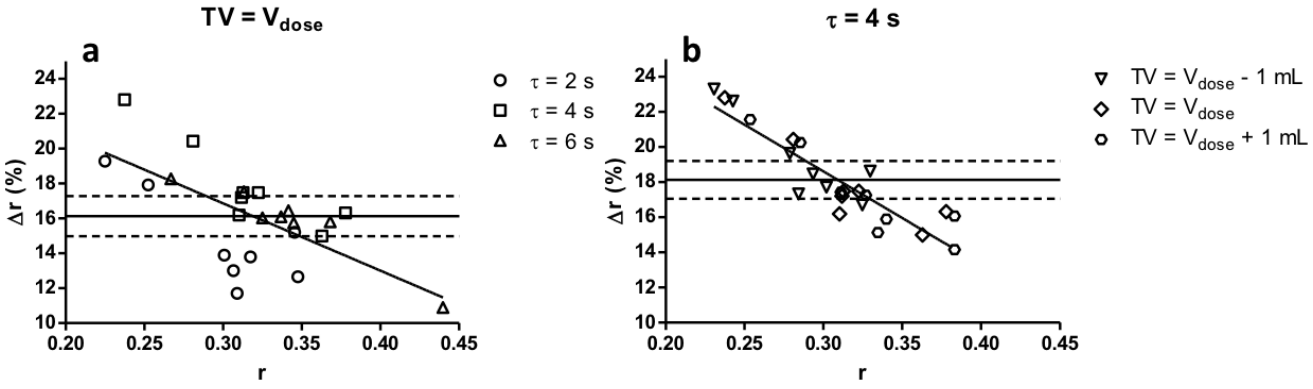

Figure 2.7: Bland-Altman plots of Δ*r* as a function of mean *r* at (**a**) *TV* = V_{dose} and (**b**) τ = 4 s. Solid horizontal lines indicate mean Δ*r* ((**a**) 16.1% and (**b**) 18.1%), dotted lines indicate upper and lower limits of 95% confidence interval ((**a**) [15.0%, 17.3%] and (**b**) [17.0%, 19.2%]), and diagonal solid lines indicate lines of best-fit ((**a**) slope = -38.6 and (**b**) slope = -53.2). The slopes of the best-fit lines are significantly non-zero ((**a**) P = 0.0004 and (**b**) $P < 10^{-4}$).

	Δ*r* (%) [95% CI]	**Slope**	**P-value (H_0: slope = 0)**
τ = 2 s, TV = V_{dose}	14.7 [12.5, 16.9]	-49.4	0.0187*
τ = 4 s, TV = V_{dose}	17.9 [15.7, 20.0]	-51.6	0.0029**
τ = 6 s, TV = V_{dose}	15.8 [14.0, 17.7]	-42.3	0.0003***
τ = 4 s, TV = V_{dose} - 1 mL	19.3 [17.2, 21.3]	-60.4	0.0044**
τ = 4 s, TV = V_{dose} + 1 mL	17.2 [15.1, 19.3]	-51.7	0.0018**

Table 2.3: Δ*r* at all τ and *TV* and slopes of regression lines for Δ*r* as a function of *r*. *P < 0.05. **P < 0.01. ***P < 0.001.

Figures 2.8a and 2.8b show Δ*r* as a function of *TV* and τ, respectively. A significant difference between the means was observed for both independent variables (F(2,7) = 6.69, P = 0.0091 for τ, and F(2,7) = 48.97, $P < 10^{-4}$ for *TV*). Post-hoc Tukey's multiple comparison test identified significant differences between all pairs of *TV* values (*TV* = V_{dose} – 1 mL and *TV* = V_{dose}, P < 0.001; *TV* = V_{dose} – 1 mL and *TV* = V_{dose} + 1 mL, P < 0.001; *TV* = V_{dose} and *TV* = V_{dose} + 1 mL, P < 0.05) and between τ = 2 s and τ = 4 s (P < 0.01).

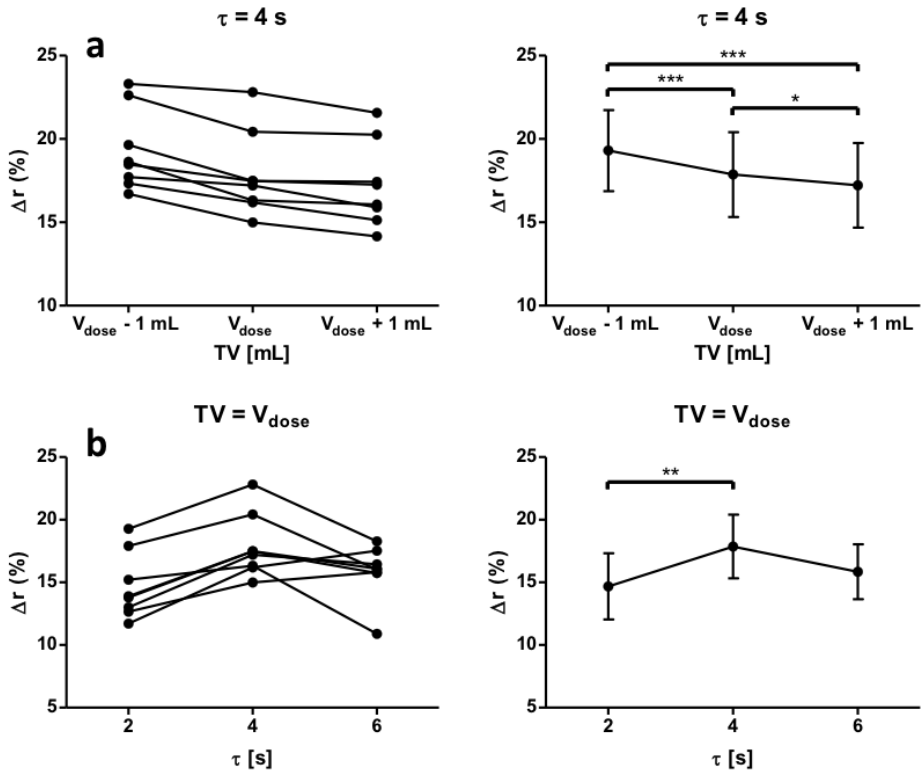

Figure 2.8: Δ*r* as a function of (**a**) *TV* and (**b**) τ. Left plots show individual trajectories for each rat and right plots show cohort mean and standard deviation. Means were significantly different for each case ((**a**) $F(2,7) = 48.97$, $P < 10^{-4}$ and (**b**) $F(2,7) = 6.69$, $P = 0.0091$). Post-hoc Tukey's multiple comparison test identified significant differences between all pairs of *TV* values and between $\tau = 2$ s and $\tau = 4$ s. $^{*}P < 0.05$. $^{**}P < 0.01$. ***$P < 0.001$.

Figure 2.9 compares the standard deviations and the skewness of the *r* and *r*' histogram distributions. The whiskers denote the minimum and maximum values. The *r*' maps demonstrated a more left-tailed distribution and thus a more negative skewness. A significant change in skewness was observed at $TV = V_{dose}$ ($\tau = 2$ s, $P < 0.05$; $\tau = 4$ s, $P < 0.05$; $\tau = 6$ s, $P < 0.01$) and at $TV = V_{dose} + 1$ mL ($P < 0.05$). A significant change in standard deviation was observed at $TV = V_{dose}$ for $\tau = 2$ s and $\tau = 6$ s ($P < 0.05$, each). Table 2.4 summarizes the average standard deviation and skewness measurements.

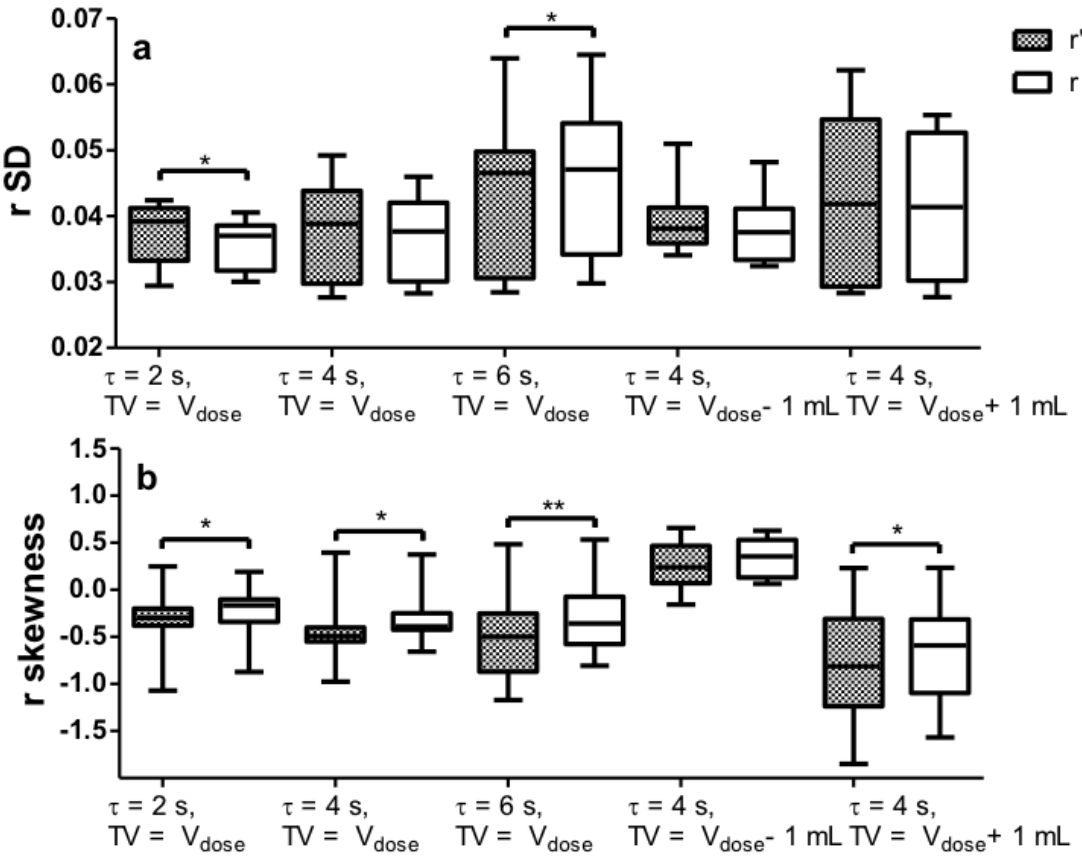

Figure 2.9: Summary of (**a**) standard deviation and (**b**) skewness of *r*' and *r* distributions measured for all rats at each combination of τ and *TV*. Whiskers indicate the range of values. $^{*}P < 0.05$. $^{**}P < 0.01$.

	Standard Deviation			**Skewness**		
	r'	*r*	P-value (H_0: *r*' = *r*)	*r*'	*r*	P-value (H_0: *r*' = *r*)
τ = 2 s, TV = V_{dose}	0.038 ± 0.005	0.036 ± 0.004	0.0173*	-0.32 ± 0.36	-0.23 ± 0.30	0.0279*
τ = 4 s, TV = V_{dose}	0.038 ± 0.004	0.037 ± 0.006	0.1540	-0.43 ± 0.38	-0.31 ± 0.30	0.0168*
τ = 6 s, TV = V_{dose}	0.044 ± 0.012	0.046 ± 0.012	0.0298*	-0.49 ± 0.50	-0.29 ± 0.41	0.0067**
τ = 4 s, TV = V_{dose} - 1 mL	0.039 ± 0.005	0.038 ± 0.005	0.0513	0.25 ± 0.26	0.34 ± 0.22	0.0536
τ = 4 s, TV = V_{dose} + 1 mL	0.043 ± 0.013	0.041 ± 0.011	0.1631	-0.79 ± 0.66	-0.67 ± 0.57	0.0258*

Table 2.4: Summary of cohort-wide mean standard deviation and skewness of histograms of *r*' and *r* (mean ± SD). $^{*}P < 0.05$. $^{**}P < 0.01$.

Validation of Eqs. 2.1 – 2.3 by measuring r in the major airways led to values of $r > 0.8$, as expected due to the near-complete gas turnover that occurs in the proximal respiratory tract. Validation of the presence of an A/P ventilation gradient led to an average gradient of -0.0408 ± 0.0257 cm^{-1} (data not shown).

2.4 Discussion

This work demonstrates the importance of considering T_1 evolution when measuring fractional ventilation (r) with HP ^{129}Xe MBW imaging. Oxygen-induced T_1 relaxation of HP ^{129}Xe gas in the lung introduces signal decay dependent on MBW breath number, $T_1(n)$. By not accounting for $T_1(n)$, an over-estimation of r of up to 19.3% was measured in the mechanically-ventilated rats. This bias (Δr) is dependent on MBW, resulting in a skewing of the distribution of r values measured by assuming a fixed T_1 toward lower r values compared to that measured by explicitly including a theoretical model of $T_1(n)$ incorporating Eqs. 2.1 and 2.2. Most notably, this bias may obscure diseased lung regions by over-estimating r in under-ventilated regions. Incorporating a model of $T_1(n)$ may therefore improve the sensitivity of MBW imaging to lung disease.

The model of $T_1(n)$, as given by Eqs. 2.1 and 2.2, was validated in four rats by explicitly measuring $T_1(n)$ for $0 \leq n \leq 2$. Figure 2.4 demonstrates that the model of $T_1(n)$ closely predicts measured $T_1(n)$ for $n \geq 1$ given $T_1(0)$ in mechanically-ventilated rats. Therefore, this model may be used to avoid having to explicitly measure $T_1(n)$ for all n, significantly reducing the time and volume of ^{129}Xe required for MBW imaging. This conclusion could be further strengthened in future by measuring $T_1(n)$ in more rats as this would improve the power of the statistical test performed on the mean difference of slopes.

Mean Δr measured at each combination of τ and TV ranged between 14.7% and 19.3%, indicating an over-estimating bias introduced by fixing T_1 at $T_1(0)$ for all n (Table 2.3). The size of the relative bias is inversely dependent on lung ventilation, and this is supported by two observations. Firstly, the negative slopes of the regression lines showed that Δr is greater at lower r. Secondly, the largest observed biases occurred at reduced TV, whereas the smallest biases on average occurred at increased TV (Fig. 2.7a). The observed bias limits the sensitivity of MBW

imaging to detecting reduced regional ventilation due to disease. This is a crucial limitation if MBW imaging is to be applied as a tool for early detection of lung disease progression.

While the means of the Δr measurements made at τ = 2 s, 4 s, and 6 s at $TV = V_{dose}$ were deemed to be significantly different, post-hoc pairwise analysis only identified a significant increase in Δr from τ = 2 s to τ = 4 s ($P < 0.01$). Nevertheless, this suggests that bias is increased when MBW imaging has a greater duration. τ should therefore be minimized while still maintaining a comfortable breathing rate. The decrease in Δr from τ = 4 s to τ = 6 s, while not significant, may be due to O_2 uptake occurring over a longer time. O_2 uptake causes a decrease in p_AO_2, which counter-acts the increase in p_AO_2 that occurs during ^{129}Xe wash-out. MBW simulations were performed to predict Δr as a function of τ for given r, $T_1(0)$, and R (grand mean values for $T_1(0)$ and R and the mean of grand mean r measured at τ = 2 s, 4 s, and 6 s at $TV = V_{dose}$ were used (Table 2.2)). Similar to what was measured, Δr was predicted to decrease beyond τ = 5.2 s. This inflection point is dependent on R, and in healthy adults, mean R is considerably lower than in rats. Rizi et al. measured a mean R of 1.55 mm Hg/s in healthy participants using HP ^{3}He MRI (93). Incorporating this value into the MBW simulation showed Δr monotonically increasing until τ = 29 s (Δr = 88.1%) - well beyond the time required for clinical MBW imaging (94). Therefore, increasing bias as a function of time is expected to pose a significant issue in clinical imaging if $T_1(n)$ is not accounted for in the analysis.

When TV was changed by ± 1 mL, a change in r and r' of roughly 0.1 was expected given an estimated lung volume of 10 mL in the rats (74). Although r and r' increased and decreased accordingly with the change in TV, the change was smaller than expected, which is evident when comparing the grand mean values in Table 2.2. As previously mentioned, this may be due to the presence of an A/P ventilation gradient (11,115) combined with the acquisition of whole-lung coronal projections. The measured A/P ventilation gradient of -0.0408 ± 0.0257 cm^{-1} closely matches the A/P gradients measured by Couch et al. in similarly ventilated rats (74). Projection imaging was used in this study, but future work should extend these techniques to 3D imaging (101) to minimize any partial-volume effects due to underlying ventilation gradients. Despite the smaller than expected change in r when TV was manipulated, the results still showed that Δr is inversely dependent on lung ventilation.

The difference between r and r' histogram distribution measurements (Fig. 2.9 and Table 2.4) suggests that the relationship between Δr and lung function is not linear. This is important because measurements such as standard deviation and skewness may be sensitive markers of ventilation heterogeneity in disease. For example, r distributions of diseased lungs may have larger standard deviations and more left-tailed skews than healthy lungs. A statistically significant change in standard deviation was observed at $TV = V_{dose}$ and τ = 2 s and 6 s (+5.6% and -4.3%, respectively). With regards to skewness, r' maps were observed to all have more left-tailed skews than r maps. Skewness, a measure of histogram asymmetry, may be a useful marker for observing lung regions that experience acute losses of function, leading to greatly reduced r values. Future studies of animal models of lung disease, such as an ovalbumin-induced model of asthma, will be important in future to investigate how ventilation heterogeneity changes with disease (118).

This study is limited by not having an accurate non-imaging measure of ventilation with which to compare. While incorporation of the model of $T_1(n)$ corrects for bias introduced by fixing T_1, a comparison of r and r' to a physiological measure of r would help with measuring the improvement in accuracy gained by incorporating $T_1(n)$. For example, in Horn et al., whole-lung r is defined as $TV/(TV + FRC)$, where FRC is the functional residual capacity (94). This would provide a degree of validation for r measured by imaging, albeit a limited one due to the loss of information on ventilation heterogeneity. In future, plethysmography should be performed to measure the lung volumes of the imaged rats.

Overall, this work demonstrates the importance of considering T_1 evolution when measuring fractional ventilation (r) with HP ^{129}Xe MBW imaging. O_2-induced T_1 relaxation of HP ^{129}Xe gas in the lungs introduces signal decay dependent on MBW breath number, $T_1(n)$. By not accounting for $T_1(n)$, an over-estimation of r of up to 19.3% in mechanically-ventilated rats was introduced, in good agreement with theoretical predictions. Bias in r (Δr) introduced by assuming a fixed T_1 (r') resulted in a non-linear positive shift of the distribution of r values. Most notably, this bias may obscure diseased lung regions by over-estimating r in under-ventilated regions. Incorporating a model of $T_1(n)$ may therefore improve the sensitivity of MBW imaging to lung disease. Before widely implementing this diagnostic tool however, greater consideration must be given for further improvements to the accuracy of MBW imaging and the challenges presented by clinical translation.

Chapter 3

3 Thesis Discussion and Future Directions

3.1 Technical Considerations

3.1.1 Confounding Sources of Signal Loss

Several non-wash-out sources of signal loss influence the accuracy of HP ^{129}Xe MBW imaging in assessing ventilation heterogeneity. As discussed in § 1.7.2, the major sources are RF depolarization, gas uptake and non-O_2-induced T_1 relaxation.

3.1.1.1 RF Depolarization

RF depolarization may be accounted for if accurate knowledge of the flip angle is known. This study incorporated a CFA approach which, while simple to implement and determine the optimal angle, causes unequal signal distribution through k-space. Centric-ordered phase encoding was employed to reduce image blurring due to the use of constant flip angles. A VFA approach, on the other hand, equally distributes signal by increasing flip angle to 90^o over the RF pulse history. Santyr et al. developed a method known as Flip Angle Variation for Offset of RF and Relaxation (FAVOR) to calibrate and implement VFA for a multiple-breath and multiple-acquisition imaging scheme. Briefly, the VFA trajectory was calibrated by increasing the transmitter gain over the RF pulse history so that the uniform response was measured over the entire trajectory. In their study, Santyr et al. showed that for HP ^{3}He multiple-breath wash-in imaging in rats, the *r* map distributions had higher means and larger standard deviations when a VFA approach was used compared to a CFA approach (91).

In the study presented in this thesis, a whole-lung measurement of flip angle was used, as it has been previously shown that a rigid transmit/receive bird-cage coil of the same size as the one used in this study provides sufficiently homogeneous B_1 to provide reliable T_1 estimates (95). In human HP gas MRI, flexible transmit/receive RF vest coils are commonly used. This may require flip angle mapping prior to MBW imaging due to B_1 inhomogeneity over the lung FOV (to successfully implement FAVOR, approximately < 3% B_1 inhomogeneity is necessary (95)). Flip angle mapping requires the patient to inhale a volume of HP ^{129}Xe identical to the volume to be

inhaled for MBW imaging. During the peak-inspiration breath-hold, two images are taken in rapid succession to minimize T_1 signal loss and ^{129}Xe uptake signal loss. The signal equation is fit to the two images on a per-voxel basis to extract a flip angle map. If the gas polarization is sufficiently high, this may be combined with T_1 mapping and MBW imaging. Essentially, during the initial breath-hold, two images in rapid succession (I1 and I2) would be acquired followed by a third image (I3) several seconds later. I1 and I2 would be used to fit for flip angle, and I2 and I3 would be used to fit for $T_1(0)$. After this breath-hold, the subject performs MBW and I3 is used as the baseline image for MBW imaging ($n = 0$). This improves upon a previously published calibration method for MBW imaging that uses two images to account for the combined effect of T_1- and RF-induced signal loss (94). Accelerated imaging techniques that utilize k-space under-sampling such as parallel imaging (119) and compressed sensing (120) may be applied. This would help to minimize the duration of the calibration phase breath-hold. Additionally, a rigid coil with a fixed geometry may be used instead of a vest coil so that B_1 inhomogeneity would be more consistent between subjects. Flip angle mapping may still be required due to the different RF coil loading (47) of each patient.

3.1.1.2 Gas Uptake

The assumption that ^{129}Xe uptake is a negligibly small confounder is based on single-breath studies and the fact that parenchymal ^{129}Xe signal is only up to roughly 2% of airspace signal (100,111). However, ^{129}Xe in the lung airspace continually dissolves into the tissue and is removed by the bloodstream after the tissue is saturated. Because of the longer timescale of MBW imaging compared to most single-breath imaging techniques, the assumption of minimal uptake may not be valid. On the other hand, the ^{129}Xe uptake rate is expected to decrease as the gas is being washed out due to Henry's Law of dynamic equilibrium (121). A study of ^{129}Xe uptake during MBW is recommended. In a proposed study, the volume of xenon gas in a gas mixture would be measured upon exhalation during MBW as a function of wash-out breath. The volume of xenon within the collected exhaled gas may be measured with a mass spectrometry method, similar to how the volume of SF_6 is measured during MBW with SF_6 (20,23). This would provide a global estimation of ^{129}Xe uptake as a function of wash-out breath, which is acceptable for diseases such as CF that have a limited effect on gas uptake heterogeneity, with the exception of very severe cases (122,123). For diseases that may heterogeneously affect gas uptake such as radiation induced lung injury, this may not be appropriate. For these cases, incorporation of imaging techniques that

utilize a model of xenon exchange, also known as MOXE, into MBW imaging may be necessary (51).

Similarly, further investigation into O_2 uptake during an MBW manoeuver is recommended. Although the measured values of *R* were in agreement with literature (107), the measurement was potentially confounded by neglecting ^{129}Xe uptake. Additionally, it was assumed that *R* remained constant throughout MBW, and this may not be the case given that p_AO_2 changes as a function of wash-out breath. In clinical imaging, fluctuating lung inflation levels may also affect *R*.

3.1.1.3 Non-O_2-induced T_1 Relaxation

To further improve $T_1(n)$ modeling and estimation of *r*, non-O_2-induced sources of T_1 relaxation should be incorporated. The rate of T_1 relaxation of ^{129}Xe in the lungs is the sum of individual rates due to different mechanisms. Diffusion through gradient magnetic fields and surface interactions are potentially the two greatest sources of T_1 relaxation following spin-exchange interactions with O_2. Therefore, T_1 relaxation may be more fully characterized as:

$$R_1 = R_{1_{O_2}} + R_{1_{\text{grad}}} + R_{1_{\text{surface}}} \quad [3.1]$$

R_1 is the rate of T_1 relaxation (i.e., $1/T_1$). $R_{1_{\text{grad}}}$ can be evaluated if the MR imaging system field strength, the field gradient magnitude along the directions orthogonal to the bore, and the diffusion coefficient of ^{129}Xe are known (86). Since a patient would be lying within the bore and along the main axis of the system's field, $R_{1_{\text{grad}}}$ is presumably negligible. If the gas reservoir from which the patient is inhaling is situated within the MR suite and outside the bore, then there may be noticeable gradient effects influencing T_1. It is recommended that the field gradients of the MRI system used for HP ^{129}Xe imaging are mapped. $R_{1_{\text{surface}}}$ is not analytically defined and is therefore much more difficult to predict. A study of T_1 that incorporates Eq. 3.1 is recommended in order to model $R_{1_{\text{surface}}}$. Precisely known mixtures of HP ^{129}Xe, O_2, and N_2 would be delivered to a rat or another appropriate model organism, and T_1 measurements would be performed at various partial pressures and inflation levels. $R_{1_{\text{surface}}}$ as a function of peak inspiratory pressure and ^{129}Xe partial pressure may then be modelled. T_1 due to surface interactions may need to be re-evaluated in models of lung disease due to physiological changes such as dried mucus in CF.

If the above confounding sources of signal loss are properly accounted for, then this would benefit $T_1(n)$ modelling and, consequently, oxygenation mapping (Eq. 1.7.3). Since the alveolar partial pressure of O_2 (p_AO_2) is dependent on the ventilation-perfusion ratio and lung structure (124), which can be greatly affected by disease, p_AO_2 mapping may be a useful tool for diagnosis and disease management.

3.1.2 Non-Hyperpolarized Alternative to HP ^{129}Xe

While this thesis investigated MBW imaging with HP ^{129}Xe, some consideration should be given to other viable tracer gases. § 1.6.2 compared the properties of ^{129}Xe to ^{3}He, another commonly used gas for HP gas MRI. While ^{3}He has an approximately three-fold larger gyromagnetic ratio than ^{129}Xe and can therefore generate greater signal at the same gas density, it is scarce, costly, and incapable of probing non-airspace regions. Inert gases containing fluorine-19 (^{19}F) have also been investigated as a viable alternative for ventilation mapping. Unlike ^{129}Xe and ^{3}He, ^{19}F can generate sufficient signal for imaging without hyperpolarization which makes the gas less costly and less difficult to prepare. ^{19}F has a high natural abundance and a large gyromagnetic ratio, comparable to ^{1}H (Table 1.1) (50,125). In addition, multiple image acquisitions may be performed in a single breath-hold because the T_1 of ^{19}F is extremely short (T_1 ~ 10 ms) (126). This improves SNR by a factor of $\sqrt{NA}$, where NA is the number of acquisitions (47). ^{19}F MBW imaging has been studied in rat models of inflammation and fibrosis, and reported r values were comparable to measurements made by Xe-CT and HP gas MRI. In this study, the imaging was performed using a mixture of SF_6 and O_2 with a pO_2 similar to air (125). Unlike HP gas MRI, O_2-induced T_1 relaxation is not a major confounder when estimating ventilation. The low cost of ^{19}F MRI and the ability to administer the gas as a mixture with O_2 makes it an attractive alternative to imaging with ^{129}Xe. However, HP ^{129}Xe MRI is still more advantageous in certain regards. Hyperpolarization provides an amplification of signal on the order of 10^5 (50), which benefits spatial resolution. ^{129}Xe can also probe the lung parenchyma and surrounding blood, unlike fluorinated gases typically used in ^{19}F MRI (e.g., C_3F_8 and SF_6). Finally, HP ^{129}Xe MRI may have an easier path to clinical approval since the fluorinated gases typically used for imaging are also greenhouses gases (127,128).

3.2 Application to Cystic Fibrosis Treatment

3.2.1 Animal Models of CF

While HP ^{129}Xe MBW imaging can be applied to observe any disease that affects ventilation heterogeneity such as asthma and COPD, the clinical motivation of this thesis is CF. Currently, there exists little research on HP ^{129}Xe MRI as a diagnostic tool for CF (56,129), and only two studies have published *r* maps from a CF patient acquired via MBW imaging, albeit using ^{3}He (94,130). To better understand how HP ^{129}Xe MBW imaging may identify changes in ventilation in CF, MBW imaging in animal models of CF should be performed. These animals may be genetically modified to reflect the change in ion transport in the airway epithelium caused by CF (e.g. induced over-expression of the epithelial sodium channel) (131). Alternatively, a researcher may opt to induce common symptoms of CF in animals, such as airway inflammation (132).

3.2.2 Correlation to PFTs

If HP gas MBW imaging eventually attains widespread clinical adoption, it will be as a complementary diagnostic tool to PFTs and other less expensive and more widely available diagnostic tools. In § 1.4.2, LCI was introduced as a measurement of ventilation that is more sensitive to CF than commonly used measurements such as FEV_1. Some studies have investigated the correlation between LCI and VDP (62,129). The relationship between LCI and *r* is arguably more meaningful given that they are both measured by MBW. Currently, only two published studies have investigated this correlation, with one using ^{3}He and the other using ^{129}Xe (130,133). Standard deviation of *r* has been shown to significantly correlate with LCI in healthy, asthmatic, and CF patients, suggesting that a greater LCI indicates greater ventilation heterogeneity (130). Neither of these studies accounted for T_1 changing as a function of wash-out breath number ($T_1(n)$) and instead fixed T_1 at the pre-wash-out value ($T_1(0)$). In future, the correlation between LCI and *r* should be re-evaluated using the model of $T_1(n)$ presented in this thesis. Evaluating *r* by instead using a fixed T_1 leads to an over-estimation of gas wash-out. Additionally, differences in LCI measured from an upright position to LCI measured from a supine position should be considered when correlating to *r* since MBW imaging is performed in a supine position (134). For example, a person breathing in a supine position tends to experience a reduction in ventilated lung volume due to the collapsing of alveoli. In other words, the person experiences reduced alveolar

recruitment (11). Compartmental analyses of LCI may also be insightful. This would involve correlating r and its distribution to LCI from different lung regions (e.g., regions experiencing "slow" versus "fast" ventilation) (135).

3.3 Clinical Translation

3.3.1 Scaling from Rat to Human Imaging

There are several factors that influence the effect of incorporating a model of $T_1(n)$ in human HP ^{129}Xe MBW imaging. Firstly, the HP ^{129}Xe dosing will be different. In the study presented in this thesis, rats were given five pre-breaths to saturate the lungs with HP ^{129}Xe. Because of the anesthetic properties of ^{129}Xe and the fact that the ^{129}Xe breath is anoxic, humans are only dosed to a fraction of their total lung capacity, typically up to one-sixth (136,137). $p_AO_2(n)$, and consequently $T_1(n)$, is therefore not expected to change as much in humans than in rats. However, clinical imaging requires longer image acquisition times to attain sufficient resolution for the larger FOV. This increases the time during which T_1 signal loss is experienced. To reduce acquisition times, accelerated imaging techniques such as parallel imaging (119) and compressed sensing (120) may be applied. Considering the differences in timescale and HP ^{129}Xe dosing, a simulation of clinical MBW imaging using the model presented in this study and timing parameters from a recent study of MBW imaging in healthy human subjects (101) was performed to predict Δr. Δr ranged from 24% to 2% for $0.1 \leq r \leq 0.9$ (data not shown). This compares to a worst-case error of <25% and an error of <15% at mean r (r = 0.37) reported previously (94). Further studies into the effect of incorporating a model of $T_1(n)$ in human HP ^{129}Xe MBW imaging are recommended.

Human MBW imaging also requires sufficiently long inter-image delay times (i.e., τ) in between the peak-inhalation breath-holds to maintain comfortable and consistent tidal breathing for patients. While the tidal volumes of the rats in this study were controlled by mechanical ventilation, consistency in humans is dependent on effort. In the Horn et al. study of HP ^{3}He MBW imaging in humans, if the tidal volume deviated by greater than 15% from the average tidal volume, then the image acquired at that breath was rejected. This meant that the model of wash-out was fit to fewer data points and more error was introduced into the estimation of r (94). Patients with poor lung function due to disease may have difficulty maintaining a regular tidal volume, particularly if the breath-holds are long. Tidal volume regulation could be assisted by incorporating

a self-gating tool. For instance, ventilator bellows attached to a monitor would allow patients to track and regulate their tidal breathing. Alternatively, if the patients were to exhale into an MR-compatible pneumotachograph (94), end-expiratory volume can be recorded and the difference from mean tidal volume could be used as a correction factor for *r*. Deviations in end-inspiratory volume could be corrected by comparing lung volumes in the acquired images. This may be especially useful for MBW imaging of very young CF patients that are incapable of following a coached breathing pattern. It is recommended that future studies investigate tidal volume deviation in MBW imaging and methods to improve breath consistency.

3.3.2 Clinical Adoption

Widespread clinical adoption will require the dissemination of technology necessary for HP ^{129}Xe MRI as well as regulatory approval. Until 2011, it has been difficult to purchase a polarizer for HP gas MRI due to lack of interest to develop the field within the companies that owned broad patents on gas hyperpolarization technologies. This has changed thanks to the recent sale of loaned polarization systems and the licensing of these patents by companies dedicated to HP gas imaging (Polarean Inc, Research Triangle Park, NC, and Xemed LLC, Durham, NH) (108). This will hopefully result in more medical research institutions establishing laboratories dedicated to HP gas MRI research. With regards to regulatory approval, agencies such as Health Canada and the Food and Drug Administration in the United States must be shown that HP gas MRI is a clinically viable diagnostic tool that leads to clear and specific improvements in therapy. This requires extensive clinical MBW imaging research, which is greatly facilitated by multi-centre collaborative efforts that can study larger patient populations than any one centre can alone. Initiatives such as the ^{129}Xe MRI Clinical Trials Consortium help to further this mission by facilitating collaboration between various laboratories that actively research HP ^{129}Xe MRI (138).

3.4 Conclusion

Early diagnosis and detection of ventilation heterogeneity is crucial to the treatment of CF because it encourages early intervention. HP ^{129}Xe MBW imaging shows great potential as an improvement upon the standard-of-care for CF patients by acting as a safe and sensitive tool for detecting regional changes in lung function. This thesis explored how O_2-induced T_1 relaxation effects, when not properly accounted for, may limit the accuracy of the imaging technique. A model of T_1 as a function of wash-out breath was developed and investigated in healthy mechanically-ventilated rats. This model corrected for an over-estimating bias in fractional ventilation of up to 19.3% introduced by assuming T_1 to be constant. By making this assumption, as has been done in previously published studies on HP gas MBW imaging, lung disease may be obscured by the over-estimation of fractional ventilation. Therefore, incorporation of the presented T_1 model improves the accuracy of MBW imaging as a tool to regionally measure lung function. In future, further work on measuring confounding sources of signal loss will continue to improve the technique's accuracy. Issues relating to clinical translation, such as corrections for tidal volume deviations during imaging, will also need to be further investigated. Ongoing collaborative research of HP ^{129}Xe MBW imaging will address these aims and greatly benefit the development, promotion, and dissemination of this imaging technique.

Bibliography

1. World Health Organization. The top 10 causes of death. 2017 [accessed 2017 Feb 10]. http://www.who.int/mediacentre/factsheets/fs310/en/

2. Public Health Agency of Canada. Economic burden of illness in Canada. 2014. 1-111 p.

3. Stephenson A, Beauchamp N. The Canadian Cystic Fibrosis Registry: 2013 Annual Report. Cystic Fibrosis Canada. 2015:1–36.

4. Ratjen F, Döring G. Cystic fibrosis. The Lancet. 2003;361(9358):681–689.

5. O'Sullivan BP, Freedman SD. Cystic fibrosis. The Lancet. 2009;373(9678):1891–1904.

6. Rogers DF. Physiology of Airway Mucus Secretion and Pathophysiology of Hypersecretion. Respiratory Care. 2007;52(9):1134–1149.

7. Davis PB, Yasothan U, Kirkpatrick P. Ivacaftor. Nature Reviews Drug Discovery. 2012;11(5):349–350.

8. Lannefors L, Button BM, McIlwaine M. Physiotherapy in infants and young children with cystic fibrosis: Current practice and future developments. Journal of the Royal Society of Medicine, Supplement. 2004;97(44):8–25.

9. Corey M, Mclaughlin FJ, Williams M, Levkon H. A comparison of survival, growth, and pulmonary function in patients with cystic fibrosis in Boston and Toronto. Journal of Clinical Epidemiology. 1988;41(6):583–591.

10. Aurora P, Bush A, Gustafsson P, Oliver C, Wallis C, Price J, Stroobant J, Carr S, Stocks J. Multiple-breath washout as a marker of lung disease in preschool children with cystic fibrosis. American Journal of Respiratory and Critical Care Medicine. 2005;171(3):249–256.

11. West J. Pulmonary Physiology and Pathophysiology: An Integrated, Case-Based Approach. Lippincott Williams & Wilkins; 2001.

12. Miller MR, Hankinson J, Brusasco V, Burgos F, Casaburi R, Coates a., Crapo R, Enright P, van der Grinten CPM, Gustafsson P, et al. Standardisation of spirometry. European Respiratory Journal. 2005;26(2):319–338.

13. Gustafsson PM, Aurora P, Lindblad A. Evaluation of ventilation maldistribution as an early indicator of lung disease in children with cystic fibrosis. European Respiratory Journal. 2003;22(6):972–979.

14. Davis S. Spirometry. Paediatric Respiratory Reviews. 2006;7(SUPPL. 1):11–13.

15. Criée CP, Sorichter S, Smith HJ, Kardos P, Merget R, Heise D, Berdel D, Köhler D, Magnussen H, Marek W, et al. Body plethysmography - Its principles and clinical use. Respiratory Medicine. 2011;105(7):959–971.

16. Quanjer PH, Cole TJ, Hall GL, Culver BH. Multi-ethnic reference values for spirometry for thee 3-95 years age range: the global lung function 2012 equations. European Respiratory Journal. 2012;40(6):1324–1343.

17. Hubble S, Macnaughton P. Tests of pulmonary function. Foundation Years. 2005;1(1):35–39.

18. Kerem E, Reisman J, Corey M, Canny GJ, Levison H. Prediction of mortality in patients with cystic fibrosis. New England Journal of Medicine. 1992;326(18):1187–1191.

19. Canada CCF. The Canadian Cystic Fibrosis Registry 2012 Annual Report. 2015:35.

20. Jensen R, Stanojevic S, Gibney K, Salazar JG, Gustafsson P, Subbarao P, Ratjen F. Multiple Breath Nitrogen Washout: A Feasible Alternative to Mass Spectrometry. PLoS ONE. 2013;8(2):1–7.

21. Subbarao P, Milla C, Aurora P, Davies JC, Davis SD, Hall GL, Heltshe S, Latzin P, Lindblad A, Pittman JE, et al. Multiple-breath washout as a lung function test in cystic fibrosis: A cystic fibrosis foundation workshop report. Annals of the American Thoracic Society. 2015;12(6):932–939.

22. Ellemunter H, Fuchs SI, Unsinn KM, Freund MC, Waltner-Romen M, Steinkamp G, Gappa M. Sensitivity of lung clearance index and chest computed tomography in early cf lung disease. Respiratory Medicine. 2010;104(12):1834–1842.

23. Aurora P, Gustafsson P, Bush a, Lindblad a, Oliver C, Wallis CE, Stocks J. Multiple breath inert gas washout as a measure of ventilation distribution in children with cystic fibrosis. Thorax. 2004;59(12):1068–1073.

24. Singer F, Houltz B, Latzin P, Robinson P, Gustafsson P. A realistic validation study of a new nitrogen multiple-breath washout system. PLoS ONE. 2012;7(4):1–8.

25. Nielsen N, Nielsen JG, Horsley AR. Evaluation of the Impact of Alveolar Nitrogen Excretion on Indices Derived from Multiple Breath Nitrogen Washout. PLoS ONE. 2013;8(9):e73335.

26. Fuchs SI, Eder J, Ellemunter H, Gappa M. Lung clearance index: Normal values, repeatability, and reproducibility in healthy children and adolescents. Pediatric Pulmonology. 2009;44(12):1180–1185.

27. Horsley A, Wild JM. Ventilation heterogeneity and the benefits and challenges of multiple breath washout testing in patients with cystic fibrosis. Paediatric Respiratory Reviews. 2015;16:15–18.

28. Fuchs SI, Gappa M, Eder J, Unsinn KM, Steinkamp G, Ellemunter H. Tracking Lung Clearance Index and chest CT in mild cystic fibrosis lung disease over a period of three years. Respiratory Medicine. 2014;108(6):865–874.

29. Hou R, Le T, Murgu SD, Chen Z, Brenner M. Recent advances in optical coherence tomography for the diagnoses of lung disorders. Expert Review of Respiratory Medicine.

2011;5(5):711–24.

30. Gargani L, Volpicelli G. How I do it: lung ultrasound. Cardiovascular Ultrasound. 2014;12(1):25.

31. Gong B, Krueger-Ziolek S, Moeller K, Schullcke B, Zhao Z. Electrical impedance tomography: functional lung imaging on its way to clinical practice? Expert review of respiratory medicine. 2015;9(6):721–37.

32. Tulek B, Kivrak AS, Ozbek S, Kanat F, Suerdem M. Phenotyping of chronic obstructive pulmonary disease using the modified Bhalla scoring system for high-resolution computed tomography. Canadian respiratory journal : journal of the Canadian Thoracic Society. 2013;20(2):91–96.

33. Prince J, Links J. Medical Imaging Signals and Systems. Upper Saddle River, NJ: Pearson Education, Inc.; 2006.

34. Kakinuma R, Moriyama N, Muramatsu Y, Gomi S, Suzuki M, Nagasawa H, Kusumoto M, Aso T, Muramatsu Y, Tsuchida T, et al. Ultra-high-resolution computed tomography of the lung: Image quality of a prototype scanner. PLoS ONE. 2015;10(9):e0137165.

35. Kong X, Sheng HX, Lu GM, Meinel FG, Dyer KT, Schoepf UJ, Zhang LJ. Xenon-enhanced dual-energy CT lung ventilation imaging: Techniques and clinical applications. American Journal of Roentgenology. 2014;202(2):309–317.

36. Sinzinger H, Rodrigues M, Kummer F. Ventilation/perfusion lung scintigraphy. Multiple applications besides pulmonary embolism. Hellenic Journal of Nuclear Medicine. 2013;16(1):50–55.

37. Fazzi Cardiothoracic CP, Dept V, Paradisa V, Fazzi P, Albertelli R, Grana M, Paggiaro PL. Lung ventilation scintigraphy in the assessment of obstructive lung diseases. Breathe. 2009;5(3):252–262.

38. Suetens P. Fundamentals of Medical Imaging. 2nd ed. New York: Cambridge University Press; 2009.

39. Gates GF, Dore EK, Markarian M, Takanaka J. Radionuclide Imaging of Airway Obstruction Following Assisted Ventilation. American Journal of Diseases of Children. 1976;130:1222–1227.

40. Venegas J, Winkler T, Harris RS. Lung Physiology and Aerosol Deposition Imaged with Positron Emission Tomography. Journal of Aerosol Medicine and Pulmonary Drug Delivery. 2013;26(1):1–8.

41. Rahmim A, Zaidi H. PET versus SPECT: strengths, limitations and challenges. Nuclear Medicine Communications. 2008;29(3):193–207.

42. Schauer DA, Linton OW. NCRP Report No. 160, Ionizing Radiation Exposure of the Population of the United States, medical exposure--are we doing less with more, and is there a

role for health physicists? Health Physics. 2009;97(1):1–5.

43. Idaho State University. Radiation and Risk. [accessed 2016 Jul 28]. http://www.physics.isu.edu/radinf/risk.htm

44. Goske MJ, Applegate KE, Boylan J, Butler PF, Callahan MJ, Coley BD, Farley S, Frush DP, Hernanz-Schulman M, Jaramillo D, et al. The "Image Gently" campaign: Increasing CT radiation dose awareness through a national education and awareness program. Pediatric Radiology. 2008;38(3):265–269.

45. Brenner DJ, Elliston CD, Hall EJ, Berdon WE. Estimated Risks of Radiation - Induced Fatal Cancer from Pediatric CT. American Journal of Roentgenology. 2001;176(2):289–296.

46. ICRP. The 2007 Recommendations of the International Commission on Radiological Protection. Annals of the ICRP. 2007;37(2–4).

47. Nishimura D. Principles of Magnetic Resonance Imaging. 1.1. Stanford University; 2010.

48. Haacke M, Brown R, Thompson M, Venkatesan R. Magnetic Resonance Imaging: Physical Principles and Sequence Design. 1st ed. Wiley-Liss; 1999.

49. Rosman K, Taylor P. Isotopic compositions of the elements 1997. Pure and Applied Chemistry. 1998;70(1):217–235.

50. Couch MJ, Blasiak B, Tomanek B, Ouriadov A V, Fox MS, Dowhos KM, Albert MS. Hyperpolarized and inert gas MRI: the future. Molecular Imaging and Biology. 2014;17(2):149–162.

51. Chang Y V., Quirk JD, Ruset IC, Atkinson JJ, Hersman FW, Woods JC. Quantification of human lung structure and physiology using hyperpolarized ^{129}Xe. Magnetic Resonance in Medicine. 2014;71(1):339–344.

52. Dournes G, Menut F, Macey J, Fayon M, Chateil J-F, Salel M, Corneloup O, Montaudon M, Berger P, Laurent F. Lung morphology assessment of cystic fibrosis using MRI with ultra-short echo time at submillimeter spatial resolution. European Radiology. 2016;26(11):3811–3820.

53. Roach DJ, Crémillieux Y, Fleck RJ, Brody AS, Serai D, Szczesniak RD, Bs SK, Clancy JP, Jason C. Ultrashort Echo-Time Magnetic Resonance Imaging Is a Sensitive Method for the Evaluation of Early Cystic Fibrosis Lung Disease. Annals of the American Thoracic Society. 2016;13(11):1923–1931.

54. Hatabu H, Alsop DC, Listerud J, Bonnet M, Gefter WB. T2* and proton density measurement of normal human lung parenchyma using submillisecond echo time gradient echo magnetic resonance imaging. European Journal of Radiology. 1999;29(3):245–252.

55. Robson MD, Gatehouse PD, Bydder M, Bydder GM. Magnetic Resonance : An Introduction to Ultrashort TE (UTE) Imaging. Journal of Computer Assisted Tomography. 2003;27(6):825–846.

56. Thomen RP, Walkup LL, Roach DJ, Cleveland ZI, Clancy JP, Woods JC. Hyperpolarized ^{129}Xe for investigation of mild cystic fibrosis lung disease in pediatric patients. Journal of Cystic Fibrosis. 2017;16(2):275–282.

57. Mugler JP, Fielden SW, Meyer CH, Altes TA, Miller GW, Stemmer A, Pfeuffer J, Kiefer B. Breath-hold UTE Lung Imaging using a Stack-of-Spirals Acquisition. Proceedings of the International Society of Magnetic Resonance in Medicine. 2015;23:1476.

58. Sá RC, Cronin M V, Henderson AC, Holverda S, Theilmann RJ, Arai TJ, Dubowitz DJ, Hopkins SR, Buxton RB, Prisk GK. Vertical distribution of specific ventilation in normal supine humans measured by oxygen-enhanced proton MRI. Journal of Applied Physiology. 2010;109(6):1950–1959.

59. Lederlin M, Bauman G, Eichinger M, Dinkel J, Brault M, Biederer J, Puderbach M. Functional MRI using Fourier decomposition of lung signal: Reproducibility of ventilation- and perfusion-weighted imaging in healthy volunteers. European Journal of Radiology. 2013;82(6):1015–1022.

60. Six JS, Hughes-Riley T, Lilburn DML, Dorkes AC, Stupic KF, Shaw DE, Morris PG, Hall IP, Pavlovskaya GE, Meersmann T. Pulmonary MRI contrast using Surface Quadrupolar Relaxation (SQUARE) of hyperpolarized ^{83}Kr. Magnetic Resonance Imaging. 2014;32(1):48–53.

61. Kirby M, Heydarian M, Svenningsen S, Wheatley A, McCormack DG, Etemad-Rezai R, Parraga G. Hyperpolarized ^{3}He Magnetic Resonance Functional Imaging Semiautomated Segmentation. Academic Radiology. 2012;19(2):141–152.

62. Kirby M, Svenningsen S, Ahmed H, Wheatley A, Etemad-Rezai R, Paterson NAM, Parraga G. Quantitative Evaluation of Hyperpolarized Helium-3 Magnetic Resonance Imaging of Lung Function Variability in Cystic Fibrosis. Academic Radiology. 2011;18(8):1006–1013.

63. xenon (n.). Online Etymology Dictionary. [accessed 2016 Oct 17]. http://www.etymonline.com/index.php?term=xenon

64. Joyce JA. Xenon: anesthesia for the 21st century. AANA Journal. 2000;68(3).

65. Nier AO. A redetermination of the relative abundances of the isotopes of neon, krypton, rubidium, xenon, and mercury. Physical Review. 1950;79(3):450–454.

66. Grasshoff C, Rudolph U, Antkowak B. Molecular and systemic mechanisms of general anaesthesia: the “multi-site and multiple mechanisms” concept. Current Opinion in Anaesthesiolgy. 2005;18(4):386–391.

67. Morgan G, Mikhail M, Murray M. Inhalational anesthetics. 4th ed. New York: McGraw-Hill; 2006. 127-145 p.

68. Hanne P, Marx T, Musati S, Santo M, Suwa K, Morita S. Xenon: uptake and costs. International Anesthesiology Clinics. 2001;39(2):43–61.

69. Muradyan I, Butler JP, Dabaghyan M, Hrovat M, Dregely I, Ruset I, Topulos GP, Frederick

E, Hatabu H, Hersman WF, et al. Single-breath xenon polarization transfer contrast (SB-XTC): implementation and initial results in healthy humans. Journal of Magnetic Resonance Imaging. 2013;37(2):457–470.

70. Goto T, Suwa K, Uezono S, Ichinose F, Uchiyama M, Morita S. The blood-gas partition coefficient of xenon may be lower than generally accepted. British Journal of Anaesthesia. 1998;80(2):255–256.

71. Chang Y V. MOXE: A model of gas exchange for hyperpolarized ^{129}Xe magnetic resonance of the lung. Magnetic Resonance in Medicine. 2013;69(3):884–890.

72. Fox MS, Ouriadov A, Thind K, Hegarty E, Wong E, Hope A, Santyr GE. Detection of radiation induced lung injury in rats using dynamic hyperpolarized ^{129}Xe magnetic resonance spectroscopy. Medical Physics. 2014;41(7):72302.

73. Kirby M, Svenningsen S, Owrangi A, Wheatley A, Farag A, Ouriadov A, Santyr GE, Etemad-Rezai R, Coxson HO, McCormack DG, et al. Imaging in Healthy Volunteers and Patients with Chronic Obstructive Pulmonary Disease. Radiology. 2012;265(2):600–610.

74. Couch MJ, Ouriadov A, Santyr GE. Regional ventilation mapping of the rat lung using hyperpolarized ^{129}Xe magnetic resonance imaging. Magnetic Resonance in Medicine. 2012;68(5):1623–1631.

75. Moller HE, Chen XJ, Saam B, Hagspiel KD, Johnson GA, Altes TA, De Lange EE, Kauczor H-U. MRI of the lungs using hyperpolarized noble gases. Magnetic Resonance in Medicine. 2002;47(6):1029–1051.

76. Bock M. Simultaneous T_2* and diffusion measurements with ^{3}He. Magnetic Resonance in Medicine. 1997;38:890–895.

77. Patyal BR, Gao JH, Williams RF. Longitudinal relaxation and diffusion measurements using magnetic resonance signals from laser-hyperpolarized ^{129}Xe nuclei. Magnetic Resonance in Medicine. 1997;126:58–65.

78. Halse M. Perspectives for Hyperpolarization in Compact NMR Spectroscopy. Trends in Analytical Chemistry. 2016;83(A):76–83.

79. Brunner E. Optimization of Pump Cells: Simulation and Experiments. In: Meersmann T, Brunner E, editors. Hyperpolarized Xenon-129 Magnetic Resonance: Concepts, Production, Techniques and Applications. Cambridge: The Royal Society of Chemistry; 2015. p. 72–85.

80. Happer W, Van Wijngaarden WA. An optical pumping primer. Hyperfine Interactions. 1987;38:435–470.

81. Wagshul ME, Chupp TE. Optical pumping of high-density Rb with a broadband dye laser and GaAlAs diode laser arrays: Application to ^{3}He polarization. Physical Review A. 1989;40(8):4447–4454.

82. Romalis M, Miron E, Cates G. Pressure broadening of Rb D_1 and D_2 lines by ^{3}He, ^{4}He, N_2,

and Xe: Line cores and near wings. Physical Review A. 1997;56(6):4569–4578.

83. Walker TG, Happer W. Spin-exchange optical pumping of noble-gas nuclei. Reviews of Modern Physics. 1997;69(2):629–642.

84. Patz S, Hersman FW, Muradian I, Hrovat MI, Ruset IC, Ketel S, Jacobson F, Topulos GP, Hatabu H, Butler JP. Hyperpolarized ^{129}Xe MRI: a viable functional lung imaging modality? European Journal of Radiology. 2007;64(3):335–344.

85. Saam B. Hyperpolarized Xenon-129 Magnetic Resonance: Concepts, Production, Techniques, and Applications. 1st ed. Brunner E, Meersmann T, editors. Cambridge: The Royal Society of Chemistry; 2015. 123 p.

86. Santyr GE, Lam WW, Parra-Robles JM, Taves TM, Ouriadov A V. Hyperpolarized noble gas magnetic resonance imaging of the animal lung: Approaches and applications. Journal of Applied Physics. 2009;105(10):102004.

87. Kuzma N, Patton B, Raman K, Happer W. Fast Nuclear Spin Relaxation in Hyperpolarized Solid ^{129}Xe. Physical Review Letters. 2002;88:147602.

88. Deninger AJ, Månsson S, Petersson JS, Pettersson G, Magnusson P, Svensson J, Fridlund B, Hansson G, Erjefeldt I, Wollmer P, et al. Quantitative measurement of regional lung ventilation using ^{3}He MRI. Magnetic Resonance in Medicine. 2002;48(2):223–232.

89. Spector ZZ, Emami K, Fischer MC, Zhu J, Ishii M, Yu J, Kadlecek S, Driehuys B, Panettieri RA, Lipson DA, et al. A small animal model of regional alveolar ventilation using HP ^{3}He MRI. Academic Radiology. 2004;11(10):1171–1179.

90. Imai H, Matsumoto H, Miyakoshi E, Okumura S, Fujiwara H, Kimura A. Regional fractional ventilation mapping in spontaneously breathing mice using hyperpolarized ^{129}Xe MRI. NMR in Biomedicine. 2015;28:24–29.

91. Santyr GE, Lam WW, Ouriadov A. Rapid and efficient mapping of regional ventilation in the rat lung using hyperpolarized ^{3}He with flip angle variation for offset of RF and relaxation (FAVOR). Magnetic Resonance in Medicine. 2008;59(6):1304–1310.

92. Emami K, Kadlecek SJ, Woodburn JM, Zhu J, Yu J, Vahdat V, Pickup S, Ishii M, Rizi RR. Improved technique for measurement of regional fractional ventilation by hyperpolarized ^{3}He MRI. Magnetic Resonance in Medicine. 2010;63(1):137–150.

93. Hamedani H, Kadlecek S, Xin Y, Siddiqui S, Gatens H, Naji J, Ishii M, Cereda M, Rossman M, Rizi R. A hybrid multibreath wash-in wash-out lung function quantification scheme in human subjects using hyperpolarized ^{3}He MRI for simultaneous assessment of specific ventilation, alveolar oxygen tension, oxygen uptake, and air trapping. Magnetic Resonance in Medicine. 2016. doi: 10.1002/mrm.26401 [Epub ahead of print].

94. Horn FC, Deppe MH, Marshall H, Parra-Robles J, Wild JM. Quantification of regional fractional ventilation in human subjects by measurement of hyperpolarized ^{3}He washout with 2D and 3D MRI. Journal of Applied Physiology. 2014;116(2):129–139.

95. Ouriadov A V, Lam WW, Santyr GE. Rapid 3-D mapping of hyperpolarized 3He spin-lattice relaxation times using variable flip angle gradient echo imaging with application to alveolar oxygen partial pressure measurement in rat lungs. Magnetic Resonance Materials in Physics, Biology and Medicine. 2009;22(5):309–318.

96. Zhao L, Mulkern R, Tseng C-H, Williamson D, Patz S, Kraft R, Walsworth RL, Jolesz FA, Albert MS. Gradient-Echo Imaging Considerations for Hyperpolarized ^{129}Xe MR. Journal of Magnetic Resonance, Series B. 1996;113:179–183.

97. Deng H, Zhong J, Ruan W, Chen X, Sun X, Ye C, Liu M, Zhou X. Constant-variable flip angles for hyperpolarized media MRI. Journal of Magnetic Resonance. 2016;263:92–100.

98. Norquay G, Leung G, Stewart NJ, Tozer GM, Wolber J, Wild JM. Relaxation and exchange dynamics of hyperpolarized ^{129}Xe in human blood. Magnetic Resonance in Medicine. 2014;311:303–311.

99. Bulter J, Mair R, Hoffmann D, Hrovat M, Rogers R, Topulos G, Walsworth R, Patz S. Measuring surface-area-to-volume ratios in soft porous materials using laser-polarized xenon interphase exchange nuclear magnetic resonance. Journal of Physics: Condensed Matter. 2002;14(13):L297–L304.

100. Ruppert K, Mata JF, Brookeman JR, Hagspiel KD, Mugler JP. Exploring lung function with hyperpolarized ^{129}Xe nuclear magnetic resonance. Magnetic Resonance in Medicine. 2004;51(4):676–687.

101. Horn FC, Rao M, Stewart NJ, Wild JM. Multiple breath washout of hyperpolarized 129Xe and 3He in human lungs with three-dimensional balanced steady-state free-precession imaging. Magnetic Resonance in Medicine. 2017;77:2288–2295.

102. Jameson CJ, Jameson AK, Hwang JK. Nuclear spin relaxation by intermolecular magnetic dipole coupling in the gas phase. ^{129}Xe in oxygen. The Journal of Chemical Physics. 1988;89(7):4074–4081.

103. Walkup LL, Woods JC. Translational applications of hyperpolarized ^{3}He and ^{129}Xe. NMR in Biomedicine. 2014;27(12):1429–1438.

104. Holmes JH, O'Halloran RL, Brodsky EK, Bley TA, Francois CJ, Velikina J V., Sorkness RL, Busse WW, Fain SB. Three-dimensional imaging of ventilation dynamics in asthmatics using multiecho projection acquisition with constrained reconstruction. Magnetic Resonance in Medicine. 2009;62(6):1543–1556.

105. Emami K, Xu Y, Hamedani H, Profka H, Kadlecek S, Xin Y, Ishii M, Rizi RR. Accelerated fractional ventilation imaging with hyperpolarized Gas MRI. Magnetic Resonance in Medicine. 2013;70(5):1353–1359.

106. Möller H, Hedlund L, Chen XJ, Carey MR, Chawla MS, Wheeler CT, Johnson GA. Measurements of hyperpolarized gas properties in the lung. Part III: ^{3}He T_1. Magnetic Resonance in Medicine. 2001;45:421–430.

107. Kadlecek S, Mongkolwisetwara P, Xin Y, Ishii M, Profka H, Emami K, Rizi R. Regional determination of oxygen uptake in rodent lungs using hyperpolarized gas and an analytical treatment of intrapulmonary gas redistribution. NMR in Biomedicine. 2011;24(10):1253-1263.

108. Mugler JP, Altes TA. Hyperpolarized ^{129}Xe MRI of the human lung. Journal of Magnetic Resonance Imaging. 2013;37(2):313–331.

109. Miller GW, Mugler JP, Altes TA, Dregely I, Ruset I, Ketel S, Hersman WF, Ruppert K. Motion-corrected pO2 mapping in human lungs using hyperpolarized Xe-129 MRI. In: Proceedings of the International Society of Magnetic Resonance in Medicine. Stockholm; 2010. p. 2558.

110. Deninger A, Eberle B, Ebert M, Grossmann T, Heil W, Kauczor H, Lauer L, Markstaller K, Otten E, Schmiedeskamp J, et al. Quantification of regional intrapulmonary oxygen partial pressure evolution during apnea by 3He MRI. Journal of Magnetic Resonance. 1999;141(2):207–216.

111. Muradyan I, Patz S, Hrovat M, Butler JP. Measurement of p_AO_2 with Hyperpolarized ^{129}Xe: Correction for Signal Decay due to Gas Exchange. Proceedings of the Internation Society of Magnetic Resonance in Medicine. 2015;23:3991.

112. Santyr GE. Transverse Relaxation of ^{129}Xe in the Lung. In: Meersmann T, Brunner E, editors. Hyperpolarized Xenon-129 Magnetic Resonance: Concepts, Production, Techniques and Applications. Cambridge, UK: The Royal Society of Chemistry; 2015. p. 394–397.

113. Parra-Robles J, Dominguez Viqueira W, Xu X, Ouriadov A, Santyr GE. Theoretical prediction and experimental measurement of the field dependence of the apparent transverse relaxation of hyperpolarized noble gases in lungs. Journal of Magnetic Resonance. 2008;192(1):85–91.

114. Dominguez-Viqueira W, Parra-Robles J, Fox M, Handler WB, Chronik BA, Santyr GE. A Variable Field Strength System for Hyperpolarized Noble Gas MR Imaging of Rodent Lungs. Concepts in Magnetic Resonance Part B (Magnetic Resonance Engineering). 2008;33B(2):124–137.

115. Hopkins SR, Henderson AC, Levin DL, Yamada K, Arai T, Buxton RB, Prisk GK. Vertical gradients in regional lung density and perfusion in the supine human lung: the Slinky effect. Journal of Applied Physiology. 2007;103(1):240–248.

116. Henkelman RM. Measurement of signal intensities in the presence of noise in MR images. Medical Physics. 1985;12(2):232–233.

117. Gudbjartsson H, Patz S. The rician distribution of noisy MRI data. Magnetic Resonance in Medicine. 1995;34(6):910–914.

118. Lilburn DML, Tatler AL, Six JS, Lesbats C, Habgood A, Porte J, Hughes-Riley T, Shaw DE, Jenkins G, Meersmann T. Investigating lung responses with functional hyperpolarized xenon-129 MRI in an ex vivo rat model of asthma. Magnetic Resonance in Medicine. 2016;76(4):1224–1235.

119. Dregely I, Ruset IC, Wiggins G, Mareyam A, Mugler JP, Altes TA, Meyer CH, Ruppert K, Wald LL, Hersman FW. 32-Channel Phased-Array Receive With Asymmetric Birdcage Transmit Coil for Hyperpolarized Xenon-129 Lung Imaging. Magnetic Resonance in Medicine. 2013;70(2):576–583.

120. Ajraoui S, Lee KJ, Deppe MH, Parnell SR, Parra-Robles J, Wild JM. Compressed sensing in hyperpolarized ^{3}He lung MRI. Magnetic Resonance in Medicine. 2010;63(4):1059–1069.

121. Henry W. Experiments on the Quantity of Gases Absorbed by Water , at Different Temperatures , and under Different Pressures. Philosophical Transactions of the Royal Society of London. 1803;93:29–42, 274–276.

122. Espiritu JD, Ruppel G, Shrestha Y, Kleinhenz ME. The diffusing capacity in adult cystic fibrosis. Respiratory Medicine. 2003;97(6):606–611.

123. Merkus PJFM, Govaere ESJ, Hop WH, Stam H, Tiddens HAWM, De Jongste JC. Preserved Diffusion Capacity in Children with Cystic Fibrosis. Pediatric Pulmonology. 2004;37(1):56–60.

124. Kadlecek SJ, Hamedani H, Xu Y, Emami K, Xin Y, Ishii M, Rizi RR. Regional Alveolar Partial Pressure of Oxygen Measurement with Parallel Accelerated Hyperpolarized Gas MRI. Academic Radiology. 2013;20(10):1224–1233.

125. Couch MJ, Fox MS, Viel C, Gajawada G, Li T, Ouriadov A V., Albert MS. Fractional ventilation mapping using inert fluorinated gas MRI in rat models of inflammation and fibrosis. NMR in Biomedicine. 2016;29(5):545–552.

126. Chang Y V., Conradi MS. Relaxation and diffusion of perfluorocarbon gas mixtures with oxygen for lung MRI. Journal of Magnetic Resonance. 2006;181(2):191–198.

127. Dervos C, Vassiliou P. Sulfur hexafluoride (SF6): global environmental effects and toxic byproduct formation. Journal of the Air & Waste Management Association. 2000;50(1):137–141.

128. Environment and Climate Change Canada. Perfluorocarbons (PFCs). 2016 [accessed 2017 Apr 26]. https://www.ec.gc.ca/toxiques-toxics/Default.asp?lang=En&n=AA329670-1

129. Kanhere N, Couch MJ, Kowalik K, Zanette B, Rayment JH, Manson D, Subbarao P, Ratjen F, Santyr G. Correlation of LCI with Hyperpolarized ^{129}Xe Magnetic Resonance Imaging in Pediatric CF Subjects. American Journal of Respiratory and Critical Care Medicine. 2017. doi: 10.1164/rccm.201611-2228LE [Epub ahead of print].

130. Horn FC, Marshall H, Siddiqui S, Horsley A, Smith L, Aldag I, Kay R, Taylor CJ, Parra-robles J, Wild JM. Ventilation heterogeneity in obstructive airways disease - comparing multi-breath washout-imaging with global measurements. Proceedings of the Internation Society of Magnetic Resonance in Medicine. 2015;23:852.

131. Zhou Z, Duerr J, Johannesson B, Schubert SC, Treis D, Harm M, Graeber SY, Dalpke A, Schultz C, Mall MA. The ENaC-overexpressing mouse as a model of cystic fibrosis lung disease. Journal of Cystic Fibrosis. 2011;10(SUPPL. 2):S172–S182.

132. Thrall RS, McCormick JR, Jack RM, McReynolds RA, Ward PA. Bleomycin-induced pulmonary fibrosis in the rat: inhibition by indomethacin. The American journal of pathology. 1979;95(1):117–130.

133. Couch MJ, Morgado F, Kanhere N, Kowalik K, Rayment J, Ratjen F, Santyr G. Hyperpolarized ^{129}Xe multiple breath washout imaging: initial experience in pediatric cystic fibrosis. Proceedings of the 2017 International Pulmonary Imaging Workshop. 2017.

134. Ramsey KA, McGirr C, Stick SM, Hall GL, Simpson SJ. Effect of posture on lung ventilation distribution and associations with structure in children with cystic fibrosis. Journal of Cystic Fibrosis. 2017. doi: 10.1016/j.jcf.2017.01.013 [Epub ahead of print].

135. Houltz B, Gilljam M, Lindblad A, Robinson PD, Gustafsson P. Slow and fast lung compartments in cystic fibrosis measured by nitrogen multiple-breath washout. Journal of Cystic Fibrosis. 2014;117:720–729.

136. Jordan BD, Wright EL. Xenon as an anesthetic agent. AANA Journal. 2010;78(5):387–392.

137. Walkup LL, Thomen RP, Akinyi TG, Watters E, Ruppert K, Clancy JP, Woods JC, Cleveland ZI. Feasibility, tolerability and safety of pediatric hyperpolarized ^{129}Xe magnetic resonance imaging in healthy volunteers and children with cystic fibrosis. Pediatric Radiology. 2016;46:1651–1662.

138. Cincinatti Children's Hospital Medical Research Center. ^{129}Xe MRI Clinical Trials Consortium. 2015 [accessed 2017 Apr 15]. https://cpir.cchmc.org/XeMRICTC

Appendix

Animal Care Committee Approval

June 23, 2016

Dear Dr. Giles Santyr,

RE: SECOND YEAR RENEWAL APPROVAL

The second year renewal for the following animal use protocol received approval at the last meeting of the Animal Care Committee:

"Micromechanical imaging of a rat model of ventilator-induced lung injury"

#35906 (Rat)

Third Year Renewal Due: June 15, 2017

- ***Request Extension: Originally a one year protocol, would now like the full 3 years, as much progress has been made. The number of rats requested for the next two years has been outlined in the renewal.***

If there are <u>any changes</u> in the information provided to the committee for this protocol, it is essential that these updates be communicated in writing to the Animal Care Committee Coordinator.

If you require any further information or assistance with this protocol, please feel free to contact me.

Sincerely,

Michelle den Hollander, M.Sc.
Animal Care Committee Coordinator
Peter Gilgan Centre for Research and Learning
Lab Animal Services, Hospital for Sick Children
Room 04.9717, Phone 416.813.5741
michelle.denhollander@sickkids.ca